

# 1 Modelling snowpack on ice surfaces with the ORCHIDEE land surface 2 model: Application to the Greenland ice sheet

3 Sylvie Charbit<sup>1</sup>, Christophe Dumas<sup>1</sup>, Fabienne Maignan<sup>1</sup>, Catherine Ottlé<sup>1</sup>, Nina Raoult<sup>2</sup>,  
4 Xavier Fettweis<sup>3</sup>, and Philippe Conesa<sup>1</sup>

5 <sup>1</sup>Laboratoire des Sciences du Climat et de l'Environnement, LSCE/IPSL, UMR 8212 CEA-CNRS-UVSQ,  
6 Université Paris-Saclay, 91191, Gif-sur-Yvette, France.

7 <sup>2</sup>Department of Mathematics and Statistics, Faculty of Environment, Science and Economy, University of Exeter,  
8 Laver Building, North Park Road, Exeter, EX4 4QE, United Kingdom.

9 <sup>3</sup>Laboratory of Climatology, Department of Geography, SPHERES, University of Liège, Liège, Belgium.

10 *Correspondence to:* Sylvie Charbit (sylvie.charbit@lsce.ipsl.fr)

11 **Abstract.** Current climate warming is accelerating mass loss from glaciers and ice sheets. In Greenland, the rates  
12 of mass changes are now dominated by changes in surface mass balance (SMB) due to increased surface melting.  
13 To improve the future sea-level rise projections, it is therefore critical to have an accurate estimate of the SMB,  
14 which depends on the representation of the processes occurring within the snowpack. The snow scheme (ES)  
15 implemented in the land surface model ORCHIDEE has not yet been adapted to ice-covered areas. Here, we  
16 present the preliminary developments we made to apply the ES model to glaciers and ice sheets. Our analysis  
17 mainly concerns the model's ability to represent ablation-related processes. At the regional scale, our results are  
18 compared to the MAR regional atmospheric model outputs and to MODIS albedo retrievals.

19 Using different albedo parameterizations, we performed offline ES simulations forced by the MAR model over  
20 the 2000-2019 period. Our results reveal a strong sensitivity of the modeled SMB components to the albedo  
21 parameterization. Results inferred with albedo parameters obtained with a manual tuning approach present a very  
22 good agreement with the MAR outputs. Conversely, with the albedo parameterization used in the standard  
23 ORCHIDEE version, runoff and sublimation were underestimated. We also tested parameters found from a  
24 previous data assimilation experiment calibrating the ablation processes using MODIS snow albedo. While these  
25 parameters greatly improve the modelled albedo over the entire ice sheet, they degrade the other model outputs  
26 compared to those obtained with the manually-tuned approach. This is likely due to the model overfitting to the  
27 calibration albedo dataset without any constraint applied to the other processes controlling the state of the  
28 snowpack. This underlines the need for performing a “multi-objective” optimisation using auxiliary observations  
29 related to snowpack internal processes. Although there is still room for further improvements, the developments  
30 reported in the present study constitute an important advance in assessing the Greenland SMB with possible  
31 extension to mountain glaciers or the Antarctic ice sheet.

## 32 1. Introduction

33 Satellite observations reveal that the Greenland ice sheet (GrIS) has been losing mass for at least three decades.  
34 Between 1992 and 2018, the net ice mass loss was estimated at  $3800 \pm 339$  Gt, corresponding to a rise in global  
35 mean sea level of  $10.6 \pm 0.9$  mm (The IMBIE team, 2020). Mass loss is driven by dynamic solid ice discharges  
36 (Enderlin et al., 2014) and by enhanced surface meltwater and runoff (Ryan et al., 2019). Over the 2000-2008  
37 period, the GrIS mass loss was equally partitioned between surface and dynamic processes (van den Broeke et al.,

38 2009). However, recent studies based on regional climate models and remote sensing observations (van den  
39 Broeke, 2016; Ryan et al., 2019; The IMBIE Team, 2020, Fox-Kemper et al., 2021) show that rates of mass change  
40 are now dominated by changes in surface mass balance (SMB), defined as the difference between mass gains (solid  
41 and liquid precipitation) and surface ablation processes (runoff, sublimation and snow erosion).

42 Besides directly impacting the global mean sea level, the GrIS is also an integral part of the Earth System (Fyke  
43 et al., 2018). As such, it is highly sensitive to climate change and in turn, has a strong influence on global climate,  
44 notably by releasing fresh water into the ocean, which leads to changes in the Atlantic meridional overturning  
45 circulation (Bakker et al., 2016; Martin et al., 2022). Surface melting may also induce changes in the local climate  
46 through the temperature-elevation feedback (Edwards et al., 2014; Sellevod et al., 2019) and the albedo effect  
47 (Box et al., 2012; Helsen et al., 2017; Riihelä et al., 2019). Finally, changes in topography produce modifications  
48 of the local and large-scale atmospheric circulations (Ridley et al., 2005; Hahn et al., 2020).

49 To capture this feedback and to reduce the uncertainties in sea-level and climate projections, a key objective of the  
50 climate-ice sheet modelling community is to incorporate ice-sheet models in Earth System Models (ESMs)  
51 (Vizcaino, 2014). Such coupled climate-ice sheet models have mainly been developed with low resolution climate  
52 models designed for long-term integrations (Kageyama et al., 2004; Charbit et al., 2005; Vizcaino et al., 2010;  
53 Roche et al., 2014). So far, only a few groups have met this goal with CMIP-like models (Vizcaino et al., 2013;  
54 Muntjewerf et al., 2020; Smith et al., 2021). A key challenge in developing such models relates to the realistic  
55 computation of SMB used as a forcing field of the ice-sheet models.

56 SMB is highly dependent on the radiative properties of snow and on the physical processes occurring within the  
57 snowpack (Helsen et al., 2017). At the surface, snow cover evolves as a function of the surface energy balance and  
58 mass exchanges with the atmosphere. In cold regions, snow melt is largely driven by shortwave radiation: Because  
59 of the high albedo value of fresh snow (0.80 – 0.90), a large fraction of shortwave radiation is reflected to the  
60 atmosphere, limiting the energy available at the surface for melting. Therefore, snow evolution is strongly  
61 dependent on the albedo. The value of snow albedo decreases when snow is ageing (i.e. in the absence of a new  
62 snowfall event) and with the snow metamorphism and liquid water content at the ice sheet's surface coming either  
63 from rainfall or from snow/ice melting. Surface water may also percolate and refreeze inside the snowpack, thereby  
64 delaying the runoff. The transformation of snow into ice depends on environmental conditions (e.g. winds, near-  
65 surface temperatures) and internal processes within the snowpack (e.g. heat conduction and vertical temperature  
66 gradient, compaction), which directly influence the grain microstructure and the snow density. All these processes  
67 affect the SMB of the ice sheet.

68 There are several ways to compute the SMB. Empirical approaches such as the positive degree-day method (Reeh,  
69 1991) have long been used to compute snow and ice melting from downscaled near-surface temperatures. This  
70 kind of approach requires little computational resources and has often been applied for past and future long-term  
71 integrations (Charbit et al., 2008; 2013; Bonelli et al., 2009; Vizcaino et al., 2010). However, such methods have  
72 been calibrated against the present state of the GrIS, raising the question as to whether they can be applied in a  
73 different climatic context from the present-day one knowing that ablation is projected to increase (van de Wal,  
74 1996; Bougamont et al., 2007). Moreover, they are not physically-based and cannot reproduce the diversity of  
75 snow processes that directly influence the SMB. Snow models implemented in general circulation models have  
76 long been based on simplified physics. They are mainly designed to resolve the seasonal and diurnal variations of  
77 heat fluxes, but with no representation of internal processes (Armstrong and Brun, 2008). By contrast, regional

78 climate models developed for polar regions generally incorporate multiple-layer energy balance snow models with  
79 a fine vertical resolution (e.g. Brun et al., 1992; Lefebre et al., 2003; Vionnet et al., 2012; Noël et al., 2018) and  
80 with detailed snow physics to simulate a variety of snowpack processes. However, due to their high computational  
81 cost, they are not often used in ESMs, despite a few rare exceptions such as the work of Punge et al. (2012) based  
82 on the implementation of a detailed snow model (Brun et al., 1992) in the atmospheric model LMDZ4 (Hourdin  
83 et al., 2006), or the Community Land Model (CLM) which includes the snow radiative transfer scheme SNICAR  
84 (Flanner and Zender, 2006) and a snow model simulating a variety of key snow processes such as the  
85 metamorphism (Lawrence et al., 2019, He et al., 2024).

86 An alternative approach consists in implementing snow models of intermediate complexity in the land surface  
87 components of ESMs (Boone and Etchevers, 2001; Dutra et al., 2010; Wang et al., 2013; Cullather et al., 2014;  
88 Decharme et al., 2016; Born et al., 2019). These models have a limited number of layers and are based on simplified  
89 representations of the main processes affecting the SMB changes, but usually do not have any explicit  
90 representation of snow metamorphism. However, they offer a good compromise between models of high  
91 complexity and simplified approaches or bulk-layer models for coupling with atmospheric models.

92 The snow module Explicit Snow (referred hereafter to as ES) implemented in the land surface model ORCHIDEE  
93 (Organising Carbon and Hydrology In Dynamic Ecosystems; Krinner et al., 2005; Chérury et al., 2020) of the  
94 IPSL-CM ESM (Boucher et al., 2020) belongs to this third class of snow models. It has been successfully evaluated  
95 against observations in Col de Porte (French Alps) and in various sites of Northern Eurasia (Wang et al., 2013).  
96 However, it has not yet been adapted to ice-covered areas. As a result, glaciers are considered as bare soils in the  
97 current ORCHIDEE version, and over ice sheets, snow is handled with the atmospheric component of IPSL-CM  
98 in a very simplistic way. Recently, we made new developments to apply the ES model to glaciers and ice sheets,  
99 with a special focus on the GrIS. These developments meet two objectives. The first one is to treat snow-related  
100 processes in IPSL-CM in a more consistent way for all surface types. The second one is to compute the SMB,  
101 taking the main processes occurring within the snowpack into account. These developments also constitute a  
102 preliminary step for the subsequent use of the computed SMB as an interface between IPSL-CM and ice-sheet  
103 models. In the following, we will refer to ORCHIDEE-ICE to deal with the version of ORCHIDEE that includes  
104 these new developments, and to ORCHIDEE to deal with the former version of the model.

105 In this study, we evaluate the computation of SMB (and its components) in the ES model. As SMB is strongly  
106 dependent on the albedo, we also examine its sensitivity to various albedo parameterizations. To achieve this, we  
107 performed offline ORCHIDEE-ICE simulations and compared our results against model outputs from the polar-  
108 oriented regional atmospheric model MARv3.11.4 (Modèle Atmosphérique Régional, Fettweis et al., 2017) and  
109 the MODIS (MODerate resolution Imaging Spectroradiometer, Hall et al., 1995; Hall and Riggs, 2016) surface  
110 albedo retrievals. The paper is organized as follows. In Section 2, we provide an extensive description of the main  
111 characteristics of the original ES model as well as changes that occurred since its early publication (Wang et al.,  
112 2013). The new developments made for applying ES to the GrIS are also presented in this section. Section 3  
113 describes the experimental setup and Section 4 provides a brief overview of the different datasets used for  
114 evaluation. The results are presented in Sections 5 and 6 and discussed in Section 7.

115

## 116 2. Model description

### 117 2.1 Snow processes in the current ORCHIDEE-AR6 model

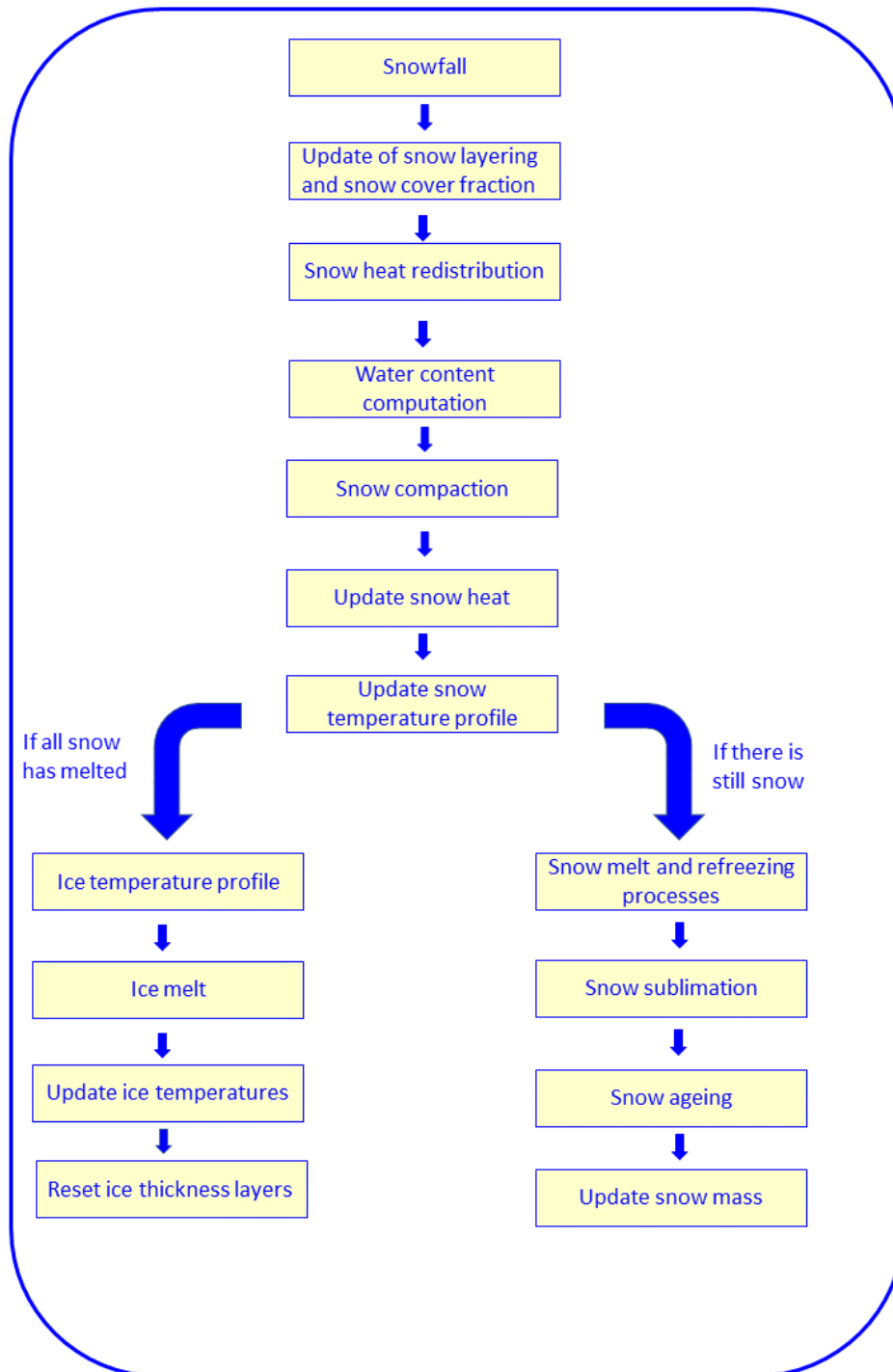
118 ORCHIDEE is the land surface component of the IPSL-CM Earth System Model (Boucher et al., 2020; Ch eruy et  
119 al., 2020) mainly developed at the French Institute Pierre Simon Laplace (IPSL). It computes both the water and  
120 energy exchanges (SECHIBA module) between land surfaces and the atmosphere at a half-hourly time step and  
121 includes carbon-related processes (STOMATE module). Within a given grid cell, land cover is represented as  
122 fractions of bare soils and vegetated areas described in terms of plant functional types (PFTs). The snow-vegetation  
123 interactions are not explicitly represented and snow is evenly distributed among the various PFTs. Soil types are  
124 prescribed according to the USDA soil texture maps (Reynolds et al., 2000). The ORCHIDEE model can be run  
125 in off-line mode, driven by atmospheric fields, or coupled with an atmospheric model. In the former ORCHIDEE  
126 version used for CMIP5 (Taylor et al., 2012), the snow scheme over glaciated surfaces was based on the bulk  
127 approach proposed by Chalita and Le Treut (1994). It consisted of a composite soil-snow model accounting for  
128 the thermal and radiative properties of snow cover (i.e. albedo and its variations with snow ageing). Snow was  
129 described as having a constant density ( $330 \text{ kg m}^{-3}$ ) and melting occurred when temperature exceeded  $0^\circ\text{C}$ . Other  
130 processes such as water percolation and refreezing were ignored, although they directly impact the water budget.  
131 This means that all liquid water coming from melting snow was leaving the snowpack as runoff.

132 For the CMIP6 exercise (Eyring et al., 2016), the bulk approach has been replaced by the ES snow scheme, which  
133 was formerly adapted to the ORCHIDEE architecture (Wang et al., 2013) from a three-layer version of the ISBA-  
134 ES scheme (Interactions between Soil, Biosphere and Atmosphere-Explicit Snow scheme; Boone and Etchevers,  
135 2001) developed at the French National Center for meteorological Research. The ES model is now used in the  
136 standard version of ORCHIDEE (version 2.0 onwards). However, it has not yet been considered for use over  
137 mountainous glaciers, which are treated as bare soils, nor over ice sheet areas, which are currently handled by the  
138 LMDZ atmospheric model (Ch eruy et al., 2020) with a very elementary snow scheme (i.e. single-layer model,  
139 constant albedo and thermal conductivity). In this section, we provide an extensive description of the snow model,  
140 including the main differences with the original ISBA-ES version (Wang et al., 2013). The new developments  
141 accounting for snow processes over ice-covered areas in the ORCHIDEE model are described in section 2.2.

142 The ES model represents the snowpack as a one-dimensional physical system (vertical coordinate  $z$ ). This means  
143 that all the lateral fluxes of mass and energy are ignored. The original version of this snowpack is discretized in  
144 three layers following the parameterization of Lynch-Stieglitz (1994), which sets the upper limits for the thickness  
145 of the first two layers at 5 and 50 cm respectively. This ensures the propagation of variations in the diurnal cycle  
146 of temperature and radiation, and enables vertical heat and density gradients, which are assumed to be larger near  
147 the surface, to be resolved correctly. Each layer is described in terms of snow density, snow age, layer thickness,  
148 heat content, snow temperature and liquid water content, with the first three variables being prognostic variables.  
149 Changes in snow mass are determined by the snowfall rate, snow melting, runoff at the base of the snowpack and  
150 sublimation at the surface. In the absence of coupling with a dynamic ice sheet model, snow mass at the surface  
151 of the ice sheet can be overestimated. Thus, to prevent excessive snow accumulation, we impose a maximum  
152 threshold of  $3000 \text{ kg m}^{-2}$  beyond which snow is artificially removed. An overview of the organization of the  
153 different subroutines of the ES snowpack model is provided in Figure 1. The description of the processes is given  
154 in the following subsections and the list of model parameters is provided in Table A1 (Appendix A).

155

## Explicit Snow



156

157 **Figure 1:** Flowchart of the new Explicit Snow scheme implemented in the ORCHIDEE-ICE model.

158

159

160

161

## 162 2.1.1 Surface processes

### 163 *Energy balance*

164 The evolution of the snowpack is primarily driven by the energy flux at the snow-atmosphere interface. A single  
165 energy balance is computed for all surface types coexisting in one grid cell. The surface energy flux ( $G_{surf}$ )  
166 available at the snow-atmosphere interface is computed from the energy balance equation:

$$167 \quad G_{surf} = SW_{net} + LW_{net} - H_L - H_S + H_{rainfall} \quad (1)$$

168  $G_{surf}$  is computed positively when it warms the soil.  $SW_{net}$  and  $LW_{net}$  are the net shortwave and longwave  
169 radiations respectively,  $H_L$  is the latent heat flux,  $H_S$  is the sensible heat flux and  $H_{rainfall}$  is the energy released  
170 by rainfall (see Eq. (14) in Boone and Etchevers, 2001). Equation (1) is used to compute the surface temperature  
171 ( $T_{surf}$ ) of the grid cell at the next time step and provides the limit condition of the surface temperature at the snow-  
172 atmosphere interface for the calculation of the snow temperature profile.

173 Above snow-covered surfaces, when  $T_{surf}$  is above the freezing temperature  $T_0$  (273.15 K), the energy excess is  
174 first used to bring the snow temperature to  $T_0$ . A surface energy flux  $G_{freezing}$  associated with the freezing  
175 temperature  $T_0$  can be computed using a similar formulation to Eq. (1). The difference between  $G_{surf}$  and  $G_{freezing}$   
176 is converted in an additional temperature expressed as:

$$177 \quad T_{snow}^{add} = T_{surf} - T_0 = \frac{G_{surf} - G_{freezing}}{c_{soil}} dt \quad (2)$$

178  $c_{soil}$  is the surface heat capacity of soil ( $J m^{-2} K^{-1}$ ) and is computed as the sum of heat capacities for snow-covered  
179 and snow-free surfaces (for both non-glaciated and glaciated areas) weighted by their respective grid cell fractions.  
180 For snow-covered surfaces, the specific heat capacity is defined as the product of snow density and the specific  
181 heat of ice ( $2106 J K^{-1} kg^{-1}$ ). If  $T_{snow}^{add}$  is greater than (or equal to) the freezing temperature, the energy excess is  
182 used for melting snow, and  $G_{surf}$  is further set to  $G_{freezing}$  for energy conservation. If the new  $G_{surf}$  value is  
183 greater than the total heat content of the snowpack, snow is entirely melted and the excess energy is transferred to  
184 the underlying soil. The energy released by snowfall is accounted for in the snowpack scheme to update the snow  
185 heat content of the snowpack after a snowfall event.

### 186 *Turbulent heat fluxes*

187 The sensible ( $H_S$ ) and latent heat ( $H_L$ ) fluxes computed for each grid cell are given respectively by:

$$188 \quad H_S = \rho_{air} q_{cdrag} U (T_{surf} - T_{air}) \quad (3)$$

$$189 \quad H_L = L_s \rho_{air} q_{cdrag} U (Q_{sat} - Q_{air}) \quad (4)$$

190 where  $\rho_{air}$  is the air density,  $T_{surf}$  and  $T_{atm}$  are the surface and the 2 m atmospheric temperatures,  $Q_{air}$  and  $Q_{sat}$   
191 are the air specific humidity at 2 m and the saturated specific humidity at the surface,  $L_s$  is the latent heat of  
192 sublimation ( $2.8345 \cdot 10^6 J kg^{-1}$ ),  $U$  is the wind speed at 10 m and  $q_{cdrag}$  is the drag coefficient computed as a  
193 function of the ice roughness length ( $z0_{ice} = 0.001 m$ ), following the Monin-Obukhov turbulence theory (Monin  
194 and Obukhov, 1954) and the parameterizations of the eddy fluxes proposed by Louis (1979).

195

196

197 ***Snow sublimation***

198 The amount of sublimation is simply deduced from the latent heat flux:

$$199 \quad S_{snow} = \frac{H_L}{L_s} \quad (5)$$

200 ***Snow cover fraction***

201 The snow cover fraction ( $F_{snow}$ ) is derived from the formulation of Niu and Yang (2007) which has been shown  
 202 to better represent the seasonal variation of the relationship between snow depth ( $Z_{snow}$ ) and snow cover fraction  
 203 thanks to its dependence on snow density:

$$204 \quad F_{snow} = \tanh\left(\frac{Z_{snow}}{2.5z_{0g} \times \left(\frac{\langle \rho_{snow} \rangle}{\rho_{min}}\right)^m}\right) \quad (6)$$

205 where  $\langle \rho_{snow} \rangle$  is the snow density averaged over the total thickness of the snowpack,  $\rho_{min}$  is the minimum snow  
 206 density (set to 50 kg m<sup>-3</sup>), that is the density of fresh snow,  $z_{0g}$  is the ground roughness length (set to 0.01 m) and  
 207  $m$  (set to 1.0 in the present study) is an adjustable parameter.

208 ***Snow albedo***

209 Compared to the early version presented in Wang et al. (2013), the albedo scheme has been modified and snow  
 210 albedo is now computed following the formulation of Chalita and Le Treut (1994):

$$211 \quad \alpha_{snow} = A_{aged} + B_{dec} \exp\left(-\frac{\tau_{snow}}{\tau_{dec}}\right) \quad (7)$$

212 where  $A_{aged}$  represents the albedo of a snow-covered surface after snow ageing (old snow) and  $B_{dec}$  is defined so  
 213 that the sum of  $A_{aged}$  and  $B_{dec}$  represents the albedo of fresh snow (i.e. maximum snow albedo).  $\tau_{dec}$  is the time  
 214 constant of the albedo decay and  $\tau_{snow}$  is the snow age and is parameterized as follows:

$$215 \quad \tau_{snow}(t + dt) = \left[\tau_{snow}(t) + \left(1 - \frac{\tau_{snow}}{\tau_{max}}\right) \times dt\right] \times \exp\left(-\frac{P_{snow}}{\delta_c}\right) + f_{age} \quad (8)$$

216 where  $\tau_{max}$  is the maximum snow age,  $P_{snow}$  is the amount of snowfall during the time interval  $dt$  and  $\delta_c$  is the  
 217 critical value of solid precipitation necessary for reducing the snow age by a factor 1/e. As the ORCHIDEE time  
 218 step is fixed to 30 mn., the snow age is almost zero in a few time steps. In addition, low surface air temperatures  
 219 found in polar regions slow down the metamorphism. This effect is accounted for with the function  $f_{age}$  expressed  
 220 as:

$$221 \quad f_{age} = \left[\frac{\left(\tau_{snow}(t) + \left(1 - \frac{\tau_{snow}}{\tau_{max}}\right) \times dt\right) \times \exp\left(-\frac{P_{snow}}{\delta_c}\right) - \tau_{snow}(t)}{1 + g_{temp}(T_{surf})}\right] \quad (9)$$

$$222 \quad g_{temp}(T_{surf}) = \left[\frac{\max(T_0 - T_{surf}, 0)}{\omega_1}\right]^{\omega_2} \quad (10)$$

223 where  $\omega_1$  and  $\omega_2$  are tuning constants. The albedo is computed for the visible and near-infrared spectral bands.  
 224 However, to compute the upward shortwave radiation, an arithmetic mean between the visible and the near-  
 225 infrared albedo is considered.

226 A single energy balance is computed for all surface types but the albedo is weighted by the different fractions of  
 227 PFTs and glaciated areas and by the snow-covered and snow-free fractions. As a result, the surface albedo ( $\alpha$ ) of

228 the grid cell is computed as the sum of snow-free albedo ( $\alpha_{snow-free}$ ) and snow-covered albedo ( $\alpha_{snow}$ ) weighted  
 229 by the fractional area of the grid cell covered by snow  $F_{snow}$  (snow-covered fraction hereafter):

$$230 \quad \alpha = F_{snow} \times \alpha_{snow} + (1 - F_{snow}) \times \alpha_{snow-free} \quad (11)$$

231 with:

$$232 \quad \alpha_{snow} = f_{ice} \times \alpha_{snow}^{ice} + \sum_{PFT} f_{PFT,i} \times \alpha_{snow}^{PFT,i} \quad (11a)$$

233 and:

$$234 \quad \alpha_{snow-free} = f_{ice} \times \alpha_{snow-free}^{ice} + \sum_{PFT} f_{PFT,i} \times \alpha_{snow-free}^{PFT,i} \quad (11b)$$

235  $f_{ice}$  and  $f_{PFT,i}$  are the grid cell fractions of ice-covered areas and the  $i^{th}$  PFT respectively;  $\alpha_{snow}^{ice}$  (resp.  $\alpha_{snow-free}^{ice}$ )  
 236 and  $\alpha_{snow}^{PFT,i}$  (resp.  $\alpha_{snow-free}^{PFT,i}$ ) are the corresponding snow albedo (resp. snow-free albedo) values.

237 Over the GrIS,  $\alpha_{snow-free}$  is given by the albedo of bare ice, prescribed to 0.6 and 0.2 for visible and near-infrared  
 238 wavelengths respectively. At the margins of the GrIS, some grid points may be only partially covered by snow or  
 239 ice, or even become totally snow-free during the melting season. It is therefore important to take these different  
 240 features into account to compute correctly the surface albedo of the GrIS.

### 241 2.1.2 Internal processes

242 When snow falls on a snow-free surface, a new snowpack is generated providing that the ground temperature is  
 243 below or equal to the freezing point. The snow mass and the heat content of the snowfall are initially distributed  
 244 evenly within the three layers. The snow density is the same for the three layers and is given by the density of the  
 245 snowfall computed as a function of wind speed and surface air temperature (Pahaut, 1976). When snowfall occurs  
 246 over an existing snowpack, fresh snow is added to the upper layer providing that the snowfall thickness is greater  
 247 than the critical threshold  $\delta_c$  (see Eq. 8). The snow thickness, density and heat content are then modified in this  
 248 layer. However, as the number of snow layers is kept fixed, redistribution of mass and heat content within the  
 249 layers is required when snow depth changes, but the total snow mass and heat content are conserved.

#### 250 *Heat conduction*

251 Solar absorption is not accounted for in the snow model. All incoming solar energy is therefore deposited at the  
 252 snow surface and distributed in deeper layers through heat conduction. The heat conduction from the surface to  
 253 the bottom of the snowpack is described by a vertical diffusion equation relating the temporal evolution of the  
 254 snow temperature in the snowpack at a depth  $z$  and the divergence of the snow heat flux  $F_C$  and is solved using an  
 255 implicit numerical scheme.

$$256 \quad \frac{\partial T_{snow}}{\partial t} = - \frac{1}{C_{snow}} \cdot \frac{\partial F_C}{\partial z} \quad (12)$$

$$257 \quad F_C = - \Lambda_s \frac{\partial T_{snow}}{\partial z} \quad (13)$$

258 with  $C_{snow}$  ( $J m^{-2} K^{-1}$ )  $\Lambda_s$  and  $T_{snow}$  being the snow heat capacity, the snow thermal conductivity ( $W m^{-1} K^{-1}$ ) and  
 259 the snow temperature respectively.

260 At the snow-atmosphere interface, the boundary condition is given by the energy balance equation ( $F_C = G_{surf}$ )  
 261 and is used in the ORCHIDEE model to compute the surface temperature.



262 Along with the thermal gradient, a water vapor diffusive flux takes place from the warmer to the colder parts of  
 263 the snowpack and sublimation or condensation may occur in the pore spaces depending on the water vapor  
 264 saturation pressure. This process is particularly significant in the Arctic because of strong temperature gradients  
 265 between soils and atmosphere and is in great part responsible for snow metamorphism. While it is explicitly  
 266 accounted for in detailed snow models, in Explicit Snow, the effect of water vapor diffusion and phase changes is  
 267 parameterized through the thermal conductivity (Sun et al., 1999). An effective thermal conductivity ( $\Lambda_{eff}$ ) is thus  
 268 expressed as the sum of empirical formulations for snow thermal conductivity ( $\Lambda_{cond}$ ) and thermal conductivity  
 269 from vapor transport ( $\Lambda_{vap}$ ), with:

$$270 \Lambda_{cond}^i = a_\lambda + b_\lambda \rho_{snow}^i \quad (14)$$

$$271 \Lambda_{vap}^i = \left( a_{\lambda v} + \frac{b_{\lambda v}}{c_{\lambda v} + T_{snow}^i} \right) \frac{P_0}{P} \quad (15)$$

272 With  $a_\lambda = 0.02 \text{ W m}^{-1} \text{ K}^{-1}$ ,  $b_\lambda = 2.5 \cdot 10^{-6} \text{ W m}^5 \text{ K}^{-1} \text{ kg}^{-2}$  (Anderson, 1976),  $a_{\lambda v} = -0.06023 \text{ W m}^{-1} \text{ K}^{-1}$ ,  $b_{\lambda v} = -2.5425$   
 273  $\text{W m}^{-1}$  and  $c_{\lambda v} = -289.99 \text{ K}$  (Yen, 1981).  $P$  is the atmospheric pressure in hPa and  $P_0 = 1000 \text{ hPa}$ . The superscripts  
 274  $i$  denote the  $i^{th}$  layer.

### 275 **Heat content**

276 The heat content is computed using the following equation:

$$277 H_{snow}^i = D_{snow}^i [C_{snow}^{v,i} (T_{snow}^i - T_f) - L_s \rho_{snow}^i] + L_f \rho_{water} W_{liq}^i \quad (16)$$

278 where  $L_f$  is the latent heat of fusion and  $\rho_{water}$  is the water density.  $H_{snow}^i$ ,  $W_{liq}^i$ ,  $D_{snow}^i$ ,  $\rho_{snow}^i$  and  $C_{snow}^{v,i}$  are  
 279 the heat and liquid contents, the depth, the density and the mean volumetric heat capacity ( $\text{J K}^{-1} \text{ m}^{-3}$ ) of the  $i^{th}$   
 280 layer.

281 After heat redistribution within the snowpack, snow temperature is diagnosed using Eq. (16), assuming no liquid  
 282 water in the snowpack. If snow temperature exceeds the freezing point, the liquid content in each layer is then  
 283 diagnosed from the snow temperature and heat content of the layer, and the temperature is then reset to the freezing  
 284 point.

### 285 **Compaction**

286 The total snow depth decreases as density increases. Changes in density occur as a result of the weight of the  
 287 overlying snow layers and under the influence of snow metamorphism. The local rate of density change in the  $i^{th}$   
 288 layer is derived from Anderson (1976):

$$289 \frac{1}{\rho_{snow}^i} \frac{\partial \rho_{snow}^i}{\partial t} = \frac{\sigma_{snow}^i}{\eta_{snow}^i (T_{snow}^i, \rho_{snow}^i)} + \psi_{snow}^i (T_{snow}^i, \rho_{snow}^i) \quad (17)$$

290 The first term of the right-hand side represents the compaction due to snow load, with  $\sigma_{snow}^i$  (Pa) being the pressure  
 291 of the overlying snow and  $\eta_{snow}^i$  the snow viscosity.

$$292 \sigma_{snow}^i = g \times M_{snow}^i$$

293 where  $g$  is the gravitational constant ( $\text{m s}^{-2}$ ) and  $M_{snow}^i$  the cumulative snow mass ( $\text{kg m}^{-2}$ ).

294 The viscosity (in Pa s) is expressed as a function of snow temperature and density (Mellor, 1964; Kojima, 1967):

$$295 \eta_{snow}^i = \eta_0 \exp[a_\eta (T_f - T_{snow}^i) + b_\eta \rho_{snow}^i] \quad (18)$$

296 with  $\eta_0 = 3.7 \times 10^7 \text{ Pa s}$ ,  $a_\eta = 8.1 \times 10^{-2} \text{ K}^{-1}$  and  $b_\eta = 1.8 \times 10^{-2} \text{ m}^3 \text{ kg}^{-1}$ .

297 The second term in the right-hand side of Eq. (17) parameterizes the effect of metamorphism which is significant  
 298 for newly fallen snow.

$$299 \quad \psi_{snow}^i = a_\psi \exp[-b_\psi \cdot (T_f - T_{snow}^i) - c_\psi \cdot \max(0, \rho_{snow}^i - \rho_\psi)] \quad (19)$$

300 The values of the parameters are the following:  $a_\psi = 2.8 \times 10^{-6} \text{ s}^{-1}$ ,  $b_\psi = 4.2 \times 10^{-2} \text{ K}^{-1}$ ,  $c_\psi = 460 \text{ m}^3 \text{ kg}^{-1}$ ,  $\rho_\psi = 150$   
 301  $\text{kg m}^{-3}$ .

302 In the model, density changes due to compaction are allowed as long as density remains below a threshold fixed  
 303 to  $750 \text{ kg m}^{-3}$ . This value was chosen because compaction becomes slower above densities between 550 and 800  
 304  $\text{kg m}^{-3}$  due to the progressive disappearance of air spaces between the snow particles (Maeno and Ebinuma, 1983).  
 305 A critical value of  $730 \text{ kg m}^{-3}$  has even been advanced by Maeno (1978). Compaction does not affect the total  
 306 mass and the heat content of the snowpack but changes the layer thicknesses. The distribution of snow heat within  
 307 the layers must therefore be updated using Eq. (16).

### 308 **Vertical temperature profile**

309 The snow temperature profile resulting from heat redistribution is then computed by solving the heat diffusion  
 310 equation using an implicit numerical scheme similar to that used for heat diffusion in the soil. The vertical  
 311 temperature profile within the snowpack is expressed as:

312 For the 1<sup>st</sup> layer:

$$313 \quad T_{snow}^1 = \left[ \frac{\lambda_{snow} \cdot C_{gr\_snow} + (T_{surf} + T_{snow}^{add})}{1 + \lambda_{snow}(1 - D_{gr\_snow})} \right] \quad (20)$$

314 For the deeper layers ( $i > 1$ ):

$$315 \quad T_{snow}^{i+1} = C_{gr\_snow} + D_{gr\_snow} \cdot T_{snow}^i \quad (21)$$

316 where  $\lambda_{snow}$ ,  $C_{gr\_snow}$ ,  $D_{gr\_snow}$  are coefficients resulting from the resolution of the numerical scheme and depend  
 317 on the snow heat capacity, thermal conductivity and characteristics of the vertical discretization. The numerical  
 318 scheme is similar to the one presented in Wang et al. (2016, see Appendix A therein) in which the temperature at  
 319 the interface between two layers is calculated as a linear interpolation according to the two nearest nodes (middle  
 320 of the layers). Diffusion therefore takes place downward and upward.

### 321 **Melting and refreezing processes**

322 If melt water is produced at the surface, it may remain in the liquid state in the uppermost layer or penetrate the  
 323 next layer where it can remain or refreeze as long as the maximum water holding capacity is not reached; otherwise,  
 324 it penetrates the lower layers.

325 The evolution of liquid water in each layer is controlled by the energy available to induce phase changes and by  
 326 the maximum water holding capacity. In the  $i^{\text{th}}$  layer, the energy used for melting snow ( $E_{snow}^i$ ) is expressed as:

$$327 \quad E_{snow}^i = \min(C_{snow}^{v,i} D_{snow}^i \times \max(0, T_{snow}^i - T_f), \max(0, D_{swe}^i - W_{liq}^i) \times L_f \rho_{water}) \quad (22)$$

328 where  $D_{swe}^i$  is the snow water equivalent in the  $i^{\text{th}}$  layer. The first term represents the available energy for phase  
 329 change in the  $i^{\text{th}}$  layer and the second term corresponds to the energy required to melt entirely the snow mass that  
 330 has not been transformed into liquid water. The maximum water holding capacity is taken from Anderson (1976):

$$331 \quad W_{max}^i = \left[ r_{min} + (r_{max} - r_{min}) \cdot \max\left(0, \frac{\rho_t - \rho_{snow}^i}{\rho_t}\right) \right] \cdot \frac{\rho_{snow}^i}{\rho_w} \cdot D_{snow}^i \quad (23)$$

332 with  $r_{min} = 0.03$ ,  $r_{max} = 0.10$  and  $\rho_t = 200 \text{ kg m}^{-3}$ .

333 Runoff ( $S_{melt}$ ) is computed as the sum of meltwater produced at the surface and the total liquid water that has  
 334 percolated down to the bottom layer and that exceeds  $W_{max}^{bottom}$ . It is thus simply given by:

$$335 \quad M_{snow} = \frac{\sum_i E_{snow}^i}{L_f} \quad (24)$$

336 At each time step, changes in layer thickness, density and liquid water content in each layer are updated as well as  
 337 changes in snow temperature due to melting or refreezing. In case of complete snow melting, the energy excess  
 338 that has not been used for phase changes is used to warm the underlying ground.

## 339 2.2 New developments

### 340 2.2.1 New snow layering scheme

341 As mentioned in Section 1, snow models of intermediate complexity are a good compromise between detailed  
 342 snow models and single-layer models. They are designed to be implemented in ESMs and, as such, should not  
 343 require excessive computational time. Although their vertical resolution is generally limited to five layers at most  
 344 (Cristea et al., 2022), several studies reported that snow models of intermediate complexity considerably improve  
 345 the representation of basic features of the snowpack and reduce biases in surface temperature when they are  
 346 compared to single-layer models (Lynch-Stieglitz, 1994; Boone and Etchevers, 2001; Dutra et al., 2012; Wang et  
 347 al., 2013). Despite these good performances, increasing the number of snow layers (with finer layers near the  
 348 surface or near the snow/ice interface) is expected to improve the modeled heat conduction within the snowpack,  
 349 the simulated temperature at the snow/ice interface, and subsequently the vertical temperature profile in the ice  
 350 and eventually the simulated SMB (Cristea et al., 2022). We therefore increased the number of snow layers from  
 351 3 to 12, following the layering scheme proposed by Decharme et al. (2016) for ISBA-ES in which the new layering  
 352 scheme is defined as:

$$353 \quad \left\{ \begin{array}{l} D_{snow}^i = \min\left(\delta_i, \frac{Z_{snow}}{12}\right) \text{ for } i \leq 5 \text{ or } i \geq 9 \\ D_{snow}^6 = 0.3d_r - \min(0, 0.3d_r - D_{snow}^5) \\ D_{snow}^7 = 0.4d_r + \min(0, 0.3d_r - D_{snow}^5) - \min(0, 0.3d_r - D_{snow}^9) \\ D_{snow}^8 = 0.3d_r - \min(0, 0.3d_r - D_{snow}^9) \\ d_r = Z_{snow} - \sum_{i=1}^5 D_{snow}^i - \sum_{i=9}^{12} D_{snow}^i \end{array} \right. \quad (25)$$

354 The  $\delta_i$  values correspond to the maximum widths of the layers 1 to 5 and 9 to 12 and are fixed to  $\delta_1 = 0.01 \text{ m}$ ,  
 355  $\delta_2 = 0.05 \text{ m}$ ,  $\delta_3 = 0.15 \text{ m}$ ,  $\delta_4 = \delta_{10} = 0.5 \text{ m}$ ,  $\delta_5 = \delta_9 = 1 \text{ m}$ ,  $\delta_{11} = 0.1 \text{ m}$ , and  $\delta_{12} = 0.02 \text{ m}$ . For very thin  
 356 snowpacks ( $Z_{snow} \leq Z_{thin} = 0.1 \text{ m}$ ), each layer has the same thickness  $\frac{Z_{thin}}{12}$ . The layer thicknesses are updated  
 357 at each time step if the first two layers ( $i = 1, 2$ ) or the bottom layer ( $i = 12$ ) become too thin  
 358 (less than  $D_{snow}^i = 0.5 \times \min\left(\delta_i, \frac{Z_{snow}}{12}\right)$ ) or too thick (larger than  $D_{snow}^i = 1.5 \times \min\left(\delta_i, \frac{Z_{snow}}{12}\right)$ ). In that  
 359 case, the snow mass and heat content are redistributed according to the new layering scheme. Otherwise, the layer

360 thicknesses at the current time step are kept to their previous values (i.e. at the previous time step). This allows to  
 361 maintain the density and thermal conductivity of fresh snow as long as the depth has not changed too much. This  
 362 enables the model to work more closely with more complex models in which new snow layers are associated with  
 363 a new snowfall event.

### 364 2.2.2 Implementation of ice layers

365 In case the snow mass has completely melted, ice melting occurs if the available energy is sufficient and contributes  
 366 to runoff. To account for the presence of ice below the snow layers, we implemented a new module in ORCHIDEE  
 367 to compute the heat diffusion and the vertical temperature distribution in the ice as well as the potential ice melting.  
 368 This module works in a similar way as the ES model and only accounts for vertical fluxes. The ice reservoir is  
 369 discretized into eight layers whose maximum thicknesses are fixed to 0.01, 0.05, 0.15, 0.5, 1, 5, 10 and 50 m. A  
 370 finer vertical spacing is imposed for the upper layers to better resolve heat conduction at the snow-ice or  
 371 atmosphere-ice interface. The large thickness of the bottom layer allows it to have an almost constant temperature  
 372 throughout the year as it has been observed at a few tens of meters depth (Patterson, 1994). Ice layers are only  
 373 implemented above an icy soil-type. If the icy soil is predominant in a given grid cell, then the entire surface  
 374 corresponding to this grid point will be considered as icy.

375 In the absence of a dynamic ice model that transports ice from the interior of the ice sheet (or glacier) to the edges,  
 376 the total ice mass may disappear entirely in the ablation zones especially in long-term simulations. To avoid such  
 377 situations, ice is considered as an infinite reservoir: melting ice contributes to runoff but, at each time step, the  
 378 amount of ice melted in the upper layers is counterbalanced by ice added at the base, and the layer thicknesses are  
 379 kept fixed to their initial value.

380 The vertical distribution of temperature is determined using the same numerical scheme as that for the snowpack.  
 381 If snow is still present over the ice soil, the temperature in the top ice layer is given by the temperature of the  
 382 bottom snow layer computed using Eq. (21). If snow has completely melted, the temperature in the first ice layer  
 383 is given by an expression similar to Eq. (20):

$$384 \quad T_{ice}^1 = \left[ \frac{\lambda_{ice} \cdot C_{gr\_ice} + (T_{surf} + T_{snow}^{add})}{1 + \lambda_{ice}(1 - D_{gr\_ice})} \right] \quad (26)$$

385 For the deeper layers, the ice temperature is expressed as follows:

$$386 \quad T_{ice}^{i+1} = C_{gr\_ice} + D_{gr\_ice} \cdot T_{ice}^i \quad (27)$$

387 Similarly to the snow coefficients (see Eqs 20 and 21),  $\lambda_{ice}$ ,  $C_{gr\_ice}$ ,  $D_{gr\_ice}$  depend on the vertical discretization  
 388 and the thermal properties of the ice. The formulations of the heat capacity ( $C_{ice}$ ) and thermal conductivity ( $\Lambda_{ice}$ )  
 389 of the ice have been taken from those used in the GRISLI ice-sheet model (Yen, 1981) and are given by:

$$390 \quad C_{ice} = \rho_{ice} (a_{ci} + b_{ci}(T_{ice} - T_0)) \quad (28)$$

$$391 \quad \Lambda_{ice} = a_{\lambda i} \exp(b_{\lambda i} \times T_0) \quad (29)$$

392 where  $T_{ice}$  is the ice temperature,  $a_{ci} = 2115.3 \text{ J K}^{-1} \text{ kg}^{-1}$ ,  $b_{ci} = 7.79293 \text{ J K}^{-2} \text{ kg}^{-1}$ ,  $a_{\lambda i} = 6.727 \text{ W m}^{-1} \text{ K}^{-1}$  and  $b_{\lambda i}$   
 393  $= -0.041 \text{ K}^{-1}$ .

394 A major difference between the hydrology of snow and ice layers lies in the fact that ice is considered as an  
 395 impermeable medium. Hence, liquid water coming from melting ice is considered to runoff instantaneously with

396 no possibility of refreezing. As a result, when the ice temperature is above the melting point, the available energy  
 397 for phase change in the  $i^{th}$  ice layer ( $J\ m^{-2}$ ) is given by:

$$398 \quad E_{ice}^i = C_{ice}^i (T_{ice}^i - T_0) D_{ice}^i \quad (30)$$

399 Similarly to  $S_{melt}$  (Eq. 24), the total amount of ice melt is given by:

$$400 \quad M_{ice} = \frac{\sum_i E_{ice}^i}{L_f} \quad (31)$$

401 and the runoff is computed as the sum of  $M_{snow}$  and  $M_{ice}$ . Given the fact that snow drift is ignored, the surface  
 402 mass balance is computed as:

$$403 \quad SMB = P_{snow} + P_{rain} - M_{snow} - M_{ice} - S_{snow} \quad (32)$$

### 404 2.2.3 Other processes in the new ES model

405 Another modification made to the ES module concerns the inclusion of rainwater percolation within the snowpack  
 406 that may refreeze at depth as long as the maximum water holding capacity is not exceeded. In case of rain-on-  
 407 snow events, we also enhanced snow ageing by a factor of two ( $f_{age} = f_{age} \times 2$ ). Although it sounds somewhat  
 408 arbitrary, we introduced this parameterization in the model to account for the effect of such events on  
 409 metamorphism and densification (Marshall et al., 1999), thereby lowering the albedo (Yang et al., 2023).

410 The snow thermal conductivity has been modified to follow a similar formulation to that used in the ISBA-ES  
 411 model (Decharme et al., 2016) and the CROCUS model (Vionnet et al., 2012) and earlier proposed by Yen (1981).  
 412 Therefore, the effective thermal conductivity in the  $i^{th}$  layer now reads as:

$$413 \quad \Lambda_{eff}^i = \left( a_{\lambda v} + \frac{b_{\lambda v}}{c_{\lambda v} + T_{snow}^i} \right) \frac{P_0}{P} + \Lambda_{ice} \left( \frac{\rho_s^i}{\rho_w} \right)^{1.88} \quad (33)$$

414 The first term of the right-hand side that parameterizes the water vapor diffusion effects ( $\Lambda_{vap}^i$ ) remains unchanged  
 415 (see Eq. 15). The second term replaces Eq. (14) used in the previous ES version (Wang et al. 2013) and corresponds  
 416 to the new formulation of the snow thermal conductivity ( $\Lambda_{cond}^i$ ). Here, the ice thermal conductivity ( $\Lambda_{ice}$ ) differs  
 417 from the value found in Decharme et al. (2016) and is given by Eq. (29).

418 Besides the new snow layering scheme and the changes mentioned in this section, all the other processes simulated  
 419 in the new ES module are treated in the same way as in the three-layer version.

## 420 3. Experimental setup

### 421 3.1 Forcing by the regional atmospheric model MAR

422 The ORCHIDEE-ICE simulations presented in this paper were driven by the atmospheric outputs of the regional  
 423 atmospheric model MAR (Fettweis et al., 2017). This approach was motivated by the fact that MAR was initially  
 424 developed for polar regions (Gallée and Schayes, 1994). Moreover, it is coupled to a land surface scheme, SISVAT  
 425 (Soil Ice Snow Vegetation Atmosphere Transfer, De Ridder and Schayes, 1997), that includes a physically-based  
 426 snowpack model derived from the multi-layered snow model CROCUS (Brun, 1989, 1992). As such, MAR has  
 427 been extensively used to simulate the present-day climate and surface mass balance of the GrIS, and compares  
 428 well to reanalyses and available data of SMB measurements (e.g. Fettweis et al. 2017, 2020; Franco et al. 2012;

429 Montgomery et al. 2020; Delhasse et al., 2020). Therefore, the use of atmospheric forcings from MAR offers a  
430 good opportunity to assess the performances of our snow model for simulating the SMB and ablation-related  
431 processes.

432 The MAR simulations (1960 – 2019) were run at a 20 km x 20 km resolution. Here, we use the version v3.11.4,  
433 identical to the version v3.11.5 for the Greenland ice sheet (Smith et al. 2023). MAR was forced every six hours  
434 at its lateral boundaries by the meteorological fields (temperature, humidity, wind, and pressure) coming from the  
435 ERA-40 (1960-1978, Uppala et al., 2005) and the ERA-Interim (1979-2019, Dee et al., 2011) reanalyses from the  
436 European Centre for Medium-Range Weather Forecasts (ECMWF). Sea surface temperatures and sea ice cover,  
437 also coming from ECMWF reanalyses, were 6-hourly prescribed.

### 438 **3.2. The ORCHIDEE-ICE simulations**

439 The ORCHIDEE-ICE simulations are run at a half-hourly time step with the same spatial resolution as the MAR  
440 outputs (20 km x 20 km). The integration domain covers the whole of Greenland. ORCHIDEE-ICE is forced every  
441 three hours by the downward shortwave and longwave radiation, the surface air temperatures and specific humidity  
442 (all at 2 meters) and the wind speed (at 10 meters), the surface pressure and the precipitation rate (split between  
443 rainfall and snowfall). Simulations are performed over the 1995-2019 period. The first five years (1995 to 1999)  
444 are used for the initialization of the snowpack and are not included in the analysis. However, to obtain reasonable  
445 thermal conditions within the ice layers, a longer time integration is required. Thus, we performed a preliminary  
446 spin-up experiment over the same 25 years to infer an initial vertical temperature profile for the subsequent  
447 ORCHIDEE-ICE simulations.

448 The name and the characteristics of the different experiments presented in this paper are summarized in Table A1.  
449 Using the experimental design described above, we first ran the ES model with three and twelve snow layers (STD-  
450 3L and STD-12L experiments respectively) to evaluate the added value of the new layering scheme. These  
451 experiments were carried out with the albedo parameters used in the CMIP6 ORCHIDEE version (Chéruy et al.,  
452 2020) and referred hereafter to as the standard snow albedo parameters.

453 Due to the strong sensitivity of the SMB to the albedo, we also conducted two additional experiments with  
454 modified values of the albedo parameters. In the ASIM-12L experiment, we used the parameters inferred from the  
455 approach of Raoult et al. (2023). This latter was based on a data assimilation experiment using the MODIS  
456 retrievals. The main goal of their study was to optimise the albedo parameters so as to improve the albedo for the  
457 ice sheet as a whole, while giving an extra weight to the edges where the greatest amount of runoff is produced.  
458 In doing this, they also succeeded in improving the model-data fit between the ORCHIDEE albedo and MODIS  
459 retrievals over the whole GrIS, and reducing the root-mean-square error (RMSE) by ~25 %. However, their work  
460 was done with a previous version of the ORCHIDEE-ICE model with only three snow layers and in which the ice  
461 layers were not implemented. Instead, ice was mimicked by a soil type whose porosity and volumetric water  
462 content were set to 98% to simulate a soil filled with frozen water.

463 The logical follow-up to the work of Raoult et al. (2023) would have been to apply the optimisation algorithm to  
464 the new version of ORCHIDEE-ICE. Since this approach is highly time-consuming, it has not yet been carried  
465 out, albeit it will be the focus of further investigations. Therefore, using the new ORCHIDEE-ICE model version,  
466 we adopted a manual tuning approach (i.e. trial-and-error method) to adjust the albedo parameters (OPT-12L  
467 experiment). This procedure consists in 1/ changing the parameter values, the new value being taken from the

468 range reported in Table 1, 2/ running the model with the new parameter values, 3/ evaluating the model  
 469 performance (in terms of SMB and its components) using statistical criteria (e.g. RMSE between MAR and  
 470 ORCHIDEE-ICE) and 4/ repeating steps 1/ to 3/ until an acceptable calibration is obtained (i.e. acceptable values  
 471 of SMB, runoff, refreezing and sublimation).

472 Finally, to assess the impact of the climatic fields used as inputs of ORCHIDEE-ICE, we performed another  
 473 experiment (ERA5-12L experiment) by forcing the model with the ERA5 reanalysis (Hersbach et al., 2020) and  
 474 using the same albedo parameters than in OPT-12L experiment.

475 **Table 1:** List of the ORCHIDEE-ICE experiments (first column) with values chosen for the different albedo  
 476 parameters (standard albedo parameters for STD-3L and STD-12L, optimized albedo parameters inferred from  
 477 Raoult et al. (2023) for ASIM-12L and manual-tuned parameters for OPT-12L and ERA-12L. Values in brackets  
 478 indicate for each parameter the range of values considered in the manual tuning approach.

Exp.	Nb of snow layers	$A_{aged}$ [0.50 - 0.70]	$B_{dec}$ [0.10 - 0.40]	$\tau_{dec}$ [1.0 - 10.0]	$\delta_c$ [0.2 - 2.0]	$\omega_1$ [1.0 - 7.0]	$\omega_2$ [0.5 - 6.0]	$\tau_{max}$ [40 - 60]	$\alpha_{ice}$ [0.30 - 0.50]
STD-3L	3	0.620	0.170	10	0.2	7	4	50	0.400
STD-12L	12	0.620	0.170	10	0.2	7	4	50	0.400
ASIM-12L	12	0.553	0.320	6.911	0.783	3.037	3.974	56.183	0.476
<b>OPT-12L</b>	<b>12</b>	<b>0.580</b>	<b>0.280</b>	<b>2.0</b>	<b>1.0</b>	<b>3</b>	<b>6</b>	<b>54</b>	<b>0.420</b>
ERA-12L	12	0.580	0.280	2.0	1.0	3	6	54	0.420

## 479 4. Methodology for the model performance evaluation

### 480 4.1 Comparison with MAR outputs

481 Our first objective is to assess the performance of the ORCHIDEE ICE model in representing the GrIS SMB. The  
 482 period under study spans over the 2000-2019 period. As mentioned in Section 3, MAR has revealed good  
 483 capabilities in simulating the SMB of present-day Greenland when compared to observational data. Therefore, at  
 484 the scale of the entire GrIS, our evaluation is made with respect to the MAR outputs (Figs 2a-5a). In all simulations  
 485 presented in this paper except ERA5-12L, the forcing fields of the ORCHIDEE-ICE model are provided by MAR  
 486 outputs. These include solid and liquid precipitation which constitute the accumulation (and the climatic)  
 487 component of the SMB. By using the MAR forcing, our analysis of the ability of ORCHIDEE-ICE to reproduce  
 488 ablation processes (runoff and sublimation) is made easier and is not biased by the use of another forcing.

### 489 4.2 Comparison with available data

490 In this study, we compared the albedo computed in ORCHIDEE-ICE with satellite-derived estimates of daily  
 491 albedo. We used Collection 6 from the MOD10A1 product (Hall et al., 1995) retrieved from the NASA space-  
 492 borne sensor MODIS. We chose this product because it has a good spatiotemporal coverage over snow-covered  
 493 areas. It is also one of the best performing products in terms of comparison with in situ data (Urraca et al., 2022,  
 494 2023). Moreover, while studies based on the previous Collection 5 reported deficiencies at latitudes higher than  
 495 70°N (Alexander et al., 2014), substantial improvements have been made to Collection 6 by using all available

496 observations for the acquisition period against only four observations per day in Collection 5  
 497 (<https://lpdaac.usgs.gov/products/mcd43d11v006/>, last access 01/22/2024). As a result, better quality retrievals are  
 498 obtained at high latitudes despite a slight negative bias (Urraca et al., 2022). To avoid inaccuracies in retrieved  
 499 data due to the presence of clouds or aircraft condensation trails, the MOD10A1 albedo product used in this study  
 500 was further processed by Box et al. (2017): data have been de-noised, gap-filled, corrected for the sun-angle bias  
 501 and validated using daily ground albedo values from the PROMICE (Programme for Monitoring of the Greenland  
 502 ice sheet, Fausto et al., 2021) and GC-net automatic weather stations (Box et al. 2017).

503 We aggregated the albedo data (500 m x 500 m) onto the MAR grid to make the comparison between MODIS data  
 504 and the ORCHIDEE-ICE outputs. In this study, we used the albedo data covering the 2000-2017 period because  
 505 data for the years 2018 and 2019 were undefined. The resulting dataset may be used to calibrate the mean  
 506 ORCHIDEE-ICE albedo, computed as the mean between the visible (from 0.4 to 0.7  $\mu\text{m}$ ) and near infrared (from  
 507 0.7 to 2.5  $\mu\text{m}$ ) bands (see Section 2).

508 As in Fettweis et al. (2020), we also evaluated the modelled SMB with the Machguth et al. (2016) SMB database.  
 509 Daily outputs are used here over 2000-2019. Modelled SMB were linearly interpolated to the measurement point  
 510 location and corrected for the elevation difference between the MAR native topography at 20km and the one  
 511 provided in the SMB database. This was done by using a space-varying SMB–elevation gradients, as proposed by  
 512 Franco et al. (2012) and Noël et al. (2016). Finally, measurements not included in the 2000–2019 period and  
 513 records located outside the 20km MAR ice mask are discarded from the evaluation.

### 514 4.3 Statistical metrics

515 To evaluate our model performances, we used statistical metrics:

516 The root-mean-square error (RMSE) has been computed using the monthly mean variables averaged over 2000-  
 517 2019 for the SMB and its components, and over 2000-2017 for the albedo. It is defined as:

$$518 \quad RMSE = \sqrt{\frac{1}{N} \sum_{i=1}^N (X_{OR}(i) - X_{MAR}(i))^2} \quad (34)$$

519 where  $X_{OR}(i)$  and  $X_{MAR}(i)$  represent the ORCHIDEE-ICE and the MAR variables respectively at each grid point  
 520  $i$ ,  $N$  is the number of unmasked grid points (i.e. related only to the ice-covered area) and  $i$  stands for the  $i^{th}$  grid  
 521 point. The RMSE is a metric widely used to compare different models but it has some shortcomings related to the  
 522 fact that higher weights are given to larger errors. We there used additional statistical criteria to provide a more in-  
 523 depth picture of our analysis. We computed the spatial RMSE (SRMSE) which gives a measure of the quadratic  
 524 difference averaged over time between values simulated by both models over the entire GrIS domain and at each  
 525 time step. Thus, by taking the temporal variations in the simulated time series into account, the spatial RMSE  
 526 makes it possible to assess the model's performance both over the entire geographical domain and over the time  
 527 period under consideration. It is computed as follows:

$$528 \quad SRMSE = \sqrt{\frac{1}{N_t \times N} \sum_{t=1}^{N_t} \sum_{i=1}^N (X_{i,OR}(t) - X_{i,MAR}(t))^2} \quad (35)$$



529  $X_{i,OR}(t)$  and  $X_{i,MAR}(t)$  are respectively the ORCHIDEE-ICE and MAR variables at each grid point  $i$  and each time  
530 step  $t$ .  $N_t$  is the number of time steps. In contrast to the RMSE, we used the daily simulated values to compute the  
531 SRMSE.

532 While the RMSE and SRMSE give an indication of the magnitude of the absolute difference between both models,  
533 it is also important to calculate the area-weighted average bias (hereafter, areal-mean bias) of each grid point in  
534 order to examine whether the model variables simulated by ORCHIDEE-ICE are underestimated (negative bias)  
535 or overestimated (positive bias). This bias (MB) is given by:

$$536 \quad MB = \frac{\sum_{i=1}^N A_i (X_{OR}(i) - X_{MAR}(i))}{\sum_{i=1}^N A_i} \quad (36)$$

537 where  $A_i$  is the surface area of each grid point.

538 Finally, we also examined the probability density functions (PDFs) and performed a Cramer-von Mises (CVM)  
539 test (Anderson, 1962) to compare the MAR and ORCHIDEE-ICE distributions of a given variable. The CVM test  
540 integrates the quadratic differences between the two models over the whole distributions (including the tails of the  
541 distributions). In this sense, it is more powerful and more sensitive to departures from the reference distribution  
542 (i.e. MAR) than the widely used Kolmogorov-Smirnov test (Stephens, 1970), which is based on the absolute value  
543 of the greatest distance between the two distributions.

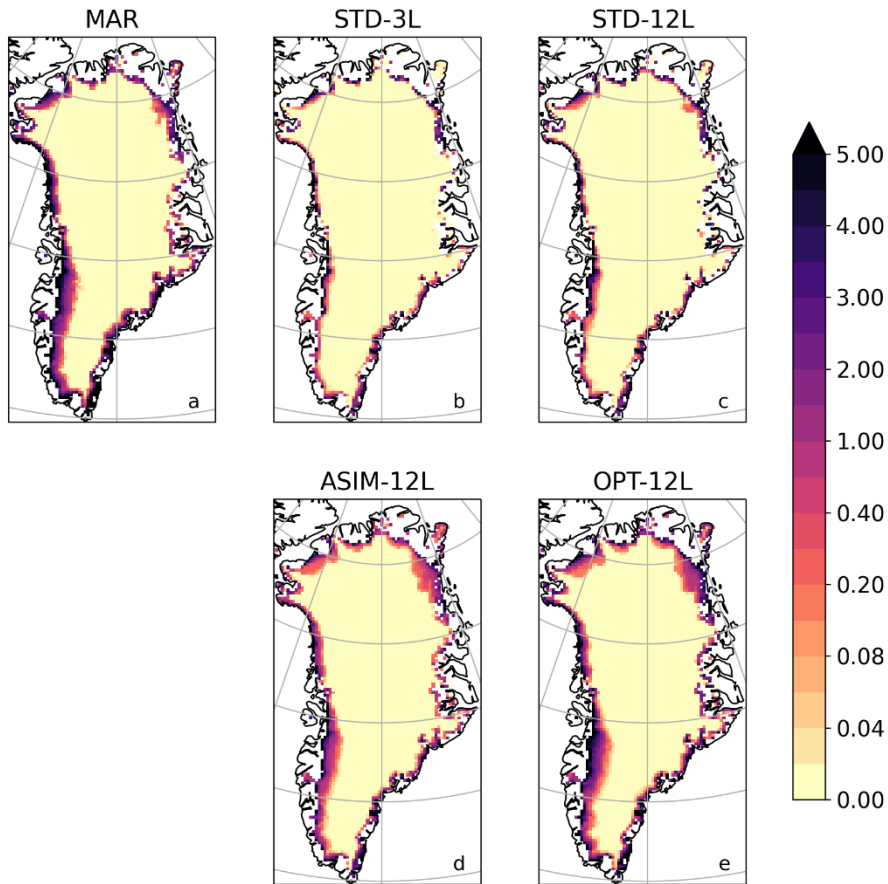
## 544 **5. Results**

### 545 **5.1 Evaluation against MAR for standard albedo parameters**

546 Figures 2 to 4 display the spatial distribution of runoff, sublimation and refreezing simulated by MAR (panels a)  
547 and by ORCHIDEE-ICE in the STD-3L (panels b) and STD-12L (panels c) experiments. The main runoff areas  
548 simulated with MAR are located on the western edge albeit, to some extent, runoff occurs in all peripheral areas  
549 of the ice sheet (Fig. 2a). Locations of the ablation zones are well represented in ORCHIDEE-ICE but are limited  
550 to a very narrow band, especially in the STD-3L simulation (Fig. 2b). Increasing the number of snow layers favors  
551 the inland expansion of the ablation areas on the western and northern margins (Fig. 2c). However, this expansion  
552 remains too restricted compared to MAR (Fig. 2a). In the ablation areas, differences in the amount of runoff exceed  
553  $1.5 \text{ mm day}^{-1}$  (Fig. S1). Integrated over the whole ice sheet (Table 2), the runoff values computed in STD-3L (152  
554  $\text{Gt yr}^{-1}$ ) and STD-12L (205  $\text{Gt yr}^{-1}$ ) experiments for the 2000-2019 period are respectively 59 % and 45 % lower  
555 compared to MAR (375  $\text{Gt yr}^{-1}$ ). As a consequence of the considerably smaller amount of runoff in ORCHIDEE-  
556 ICE, and thus of surface meltwater, refreezing is also much lower (Table 2) and less extended (Figs. 3a-c)  
557 compared to MAR. It can be noted, however, that the disagreement is less pronounced with the STD-12L  
558 experiment (Fig. S2), which underlines the benefit of increasing the number of snow layers.

559

Runoff 2000-2019 (mm day<sup>-1</sup>)



560

561 **Figure 2:** Spatial distribution of the runoff (in mm day<sup>1</sup>) averaged over the 2000-2019 period and simulated with  
562 MAR (a) and the ORCHIDEE-ICE model (b-e) using: the three-layer snow scheme and the standard albedo  
563 parameters (b), the twelve-layer snow scheme and the standard albedo parameters (c), the twelve-layer snow  
564 scheme and the albedo parameters optimised using a data assimilation technique (Raoult et al., 2023) and a  
565 previous version of the ORCHIDEE-ICE model (d), the twelve-layer snow scheme and the albedo parameters  
566 obtained after manual tuning (e).

567

568 **Table 2:** Simulated values of SMB, runoff, sublimation and refreezing integrated over the entire Greenland ice  
569 sheet and averaged over the 2000-2019 period (2<sup>nd</sup> column). Evaluation of simulated SMB and SMB components  
570 is done with respect to MAR outputs using values of root-mean-square error (3<sup>rd</sup> column), areal mean bias and  
571 (4<sup>th</sup> column) and spatial root-mean-square error (5<sup>th</sup> column).

Experiments	SMB (Gt yr <sup>-1</sup> )	RMSE (in mm day <sup>-1</sup> )	Areal mean bias (in mm day <sup>-1</sup> )	Spatial RMSE (in mm day <sup>-1</sup> )
<b>MAR</b>	<b>286</b>			
STD-3L	504	0.976	0.351	3.050
STD-12L	450	0.786	0.264	2.809
ASIM-12L	466	0.706	0.290	2.602
<b>OPT-12L</b>	<b>301</b>	<b>0.464</b>	<b>0.024</b>	<b>2.530</b>
ERA5-12L	352			

Experiments	Runoff (Gt yr <sup>-1</sup> )	RMSE (in mm day <sup>-1</sup> )	Areal mean bias (in mm day <sup>-1</sup> )	Spatial RMSE (in mm day <sup>-1</sup> )
<b>MAR</b>	<b>375</b>			
STD-3L	152	1.107	- 0.357	3.157
STD-12L	205	0.922	- 0.272	2.900
ASIM-12L	217	0.829	- 0.254	2.639
<b>OPT-12L</b>	<b>336</b>	<b>0.592</b>	<b>-0.063</b>	<b>2.539</b>
ERA5-12L	273			

Experiments	Sublimation (Gt yr <sup>-1</sup> )	RMSE (in mm day <sup>-1</sup> )	Areal mean bias (in mm day <sup>-1</sup> )	Spatial RMSE (in mm day <sup>-1</sup> )
<b>MAR</b>	<b>82</b>			
STD-3L	32	1.000	- 0.081	0.200
STD-12L	33	0.096	- 0.079	0.203
ASIM-12L	5	0.134	- 0.124	0.226
OPT-12L	52	0.077	- 0.049	0.274
ERA5-12L	89			

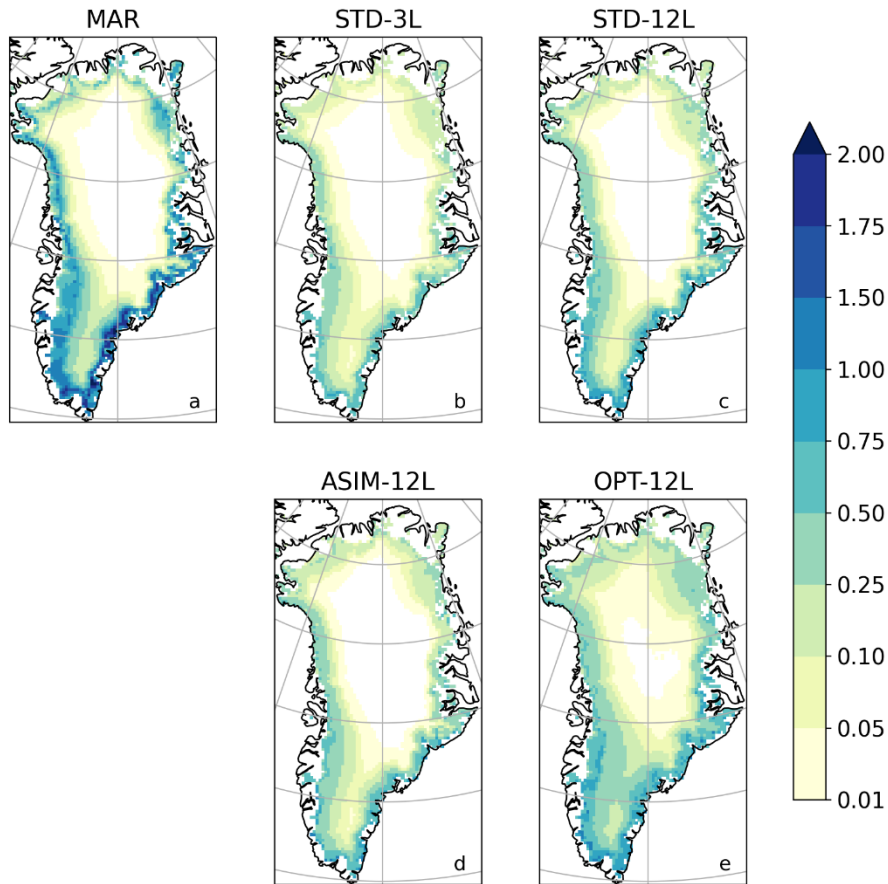
Experiments	Refreezing (Gt yr <sup>-1</sup> )	RMSE (in mm day <sup>-1</sup> )	Areal mean bias (in mm day <sup>-1</sup> )	Spatial RMSE (in mm day <sup>-1</sup> )
<b>MAR</b>	<b>186</b>			
STD-3L	72	0.336	- 0.183	1.254
STD-12L	104	0.269	-0.131	1.134
ASIM-12L	90	0.313	- 0.155	1.182
<b>OPT-12-L</b>	<b>158</b>	<b>0.240</b>	<b>-0.046</b>	<b>1.316</b>
ERA5-12L				

572

573

574

Refreezing 2000-2019 ( $\text{mm day}^{-1}$ )



575

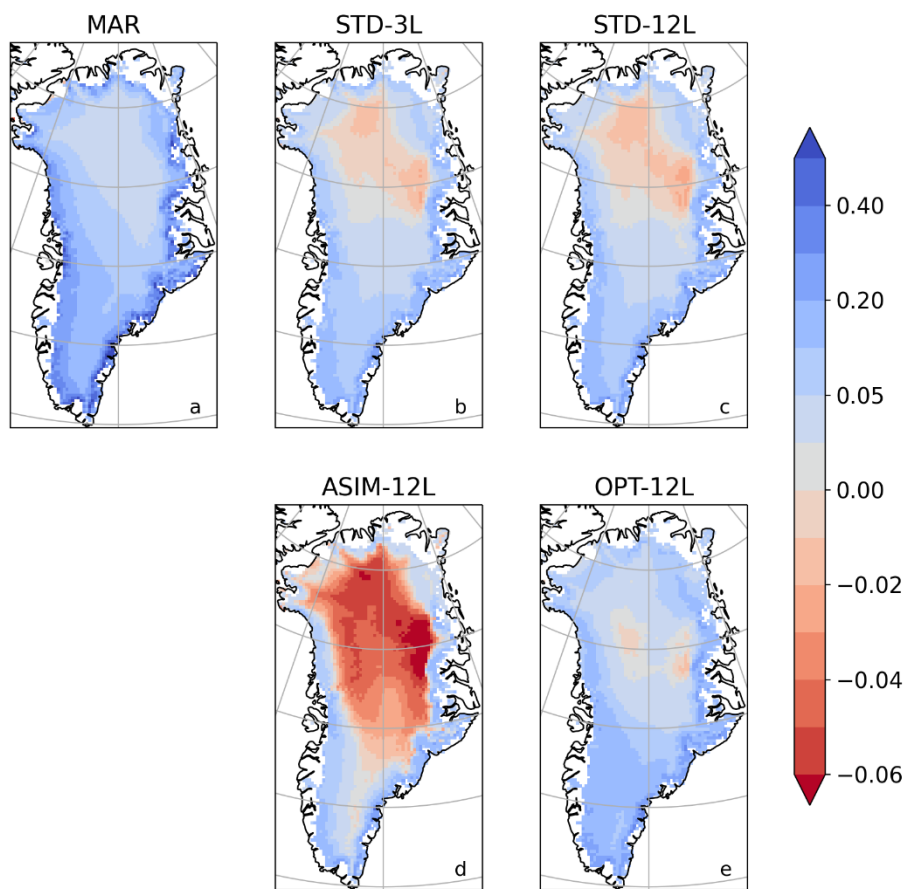
576 **Figure 3:** Same as Figure 2 for the simulated refreezing (in  $\text{mm day}^{-1}$ ).

577 Large differences between MAR and ORCHIDEE-ICE also arise regarding sublimation ( $32$  and  $33 \text{ Gt yr}^{-1}$  in the  
 578 STD-3L and STD-12L experiments respectively, against  $82 \text{ Gt yr}^{-1}$  for the 2000-2019 period in MAR). This feature  
 579 concerns the entire ice sheet but is even more striking in peripheral areas (Figs 4 and S3). In central Greenland,  
 580 differences are smaller, but ORCHIDEE-ICE simulates a little condensation (Fig. 4) whereas MAR does not.

581 The differences in simulated runoff and in sublimation between MAR and ORCHIDEE-ICE translate into  
 582 overestimated SMB values simulated with ORCHIDEE-ICE ( $504$  and  $450 \text{ Gt yr}^{-1}$  in STD-3L and STD-12L against  
 583  $286 \text{ Gt yr}^{-1}$  in MAR; see also Figs. 5 and S4). Since inland regions are dominated by the accumulation signal,  
 584 which is provided by the MAR outputs, the SMB anomalies are primarily driven by differences in the ablation  
 585 components occurring at the edges of the ice sheet, and exceed  $2 \text{ mm day}^{-1}$  in most parts of the western and  
 586 southeastern margins.

587 An important conclusion that can be drawn from these results is that the use of a better resolved snow layering  
 588 scheme (twelve-layer as opposed to a three-layer snow scheme) reduces the mismatch between MAR and  
 589 ORCHIDEE-ICE. This is mainly illustrated by the integrated SMB and runoff values which are respectively  $\sim 35\%$   
 590 lower and  $\sim 11\%$  higher in STD-12L, translating into reductions of RMSE values ( $\sim 19\%$  and  $\sim 17\%$  for SMB and  
 591 runoff respectively, see Table2), areal mean bias ( $\sim 25\%$  and  $\sim 24\%$  respectively), and, to a lesser extent, of the  
 592 spatial RMSE ( $\sim 8\%$  for both SMB and runoff). Nevertheless, the differences with MAR are still too large for the  
 593 model to be used as a reliable tool to compute the GrIS SMB.

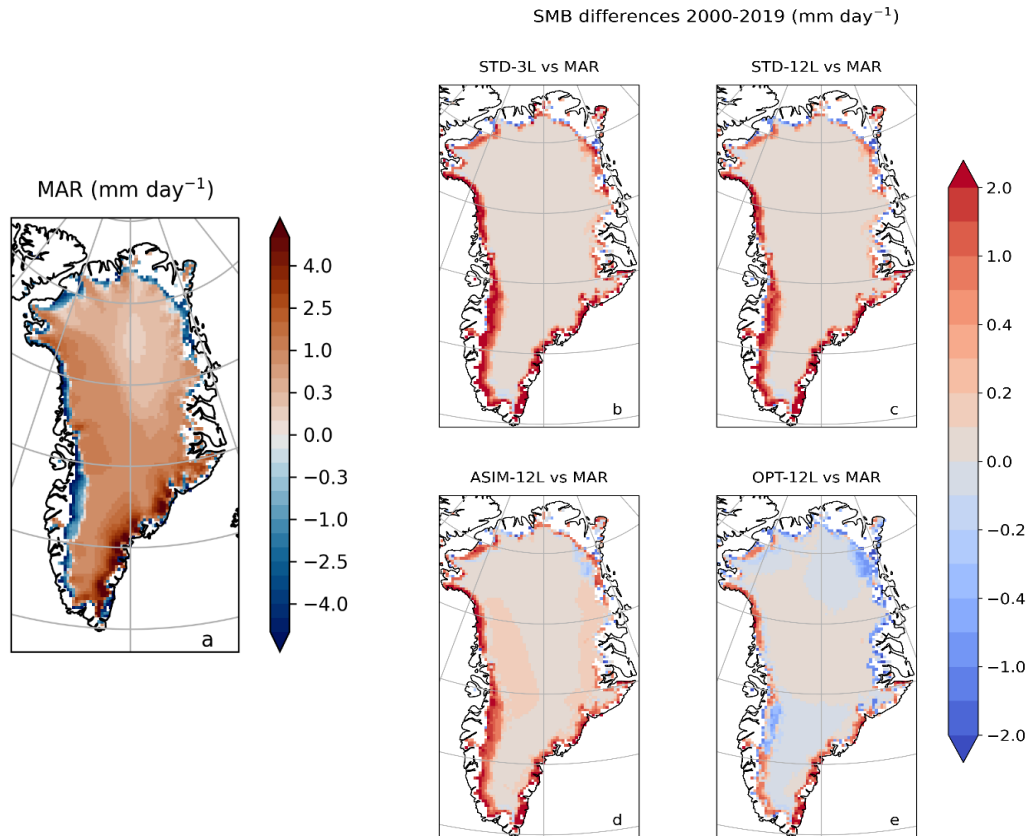
Sublimation 2000-2019 (mm day<sup>-1</sup>)



594

595 **Figure 4:** Same as Figure 2 for the simulated sublimation (in mm day<sup>-1</sup>). Negative values indicate condensation.

596



597

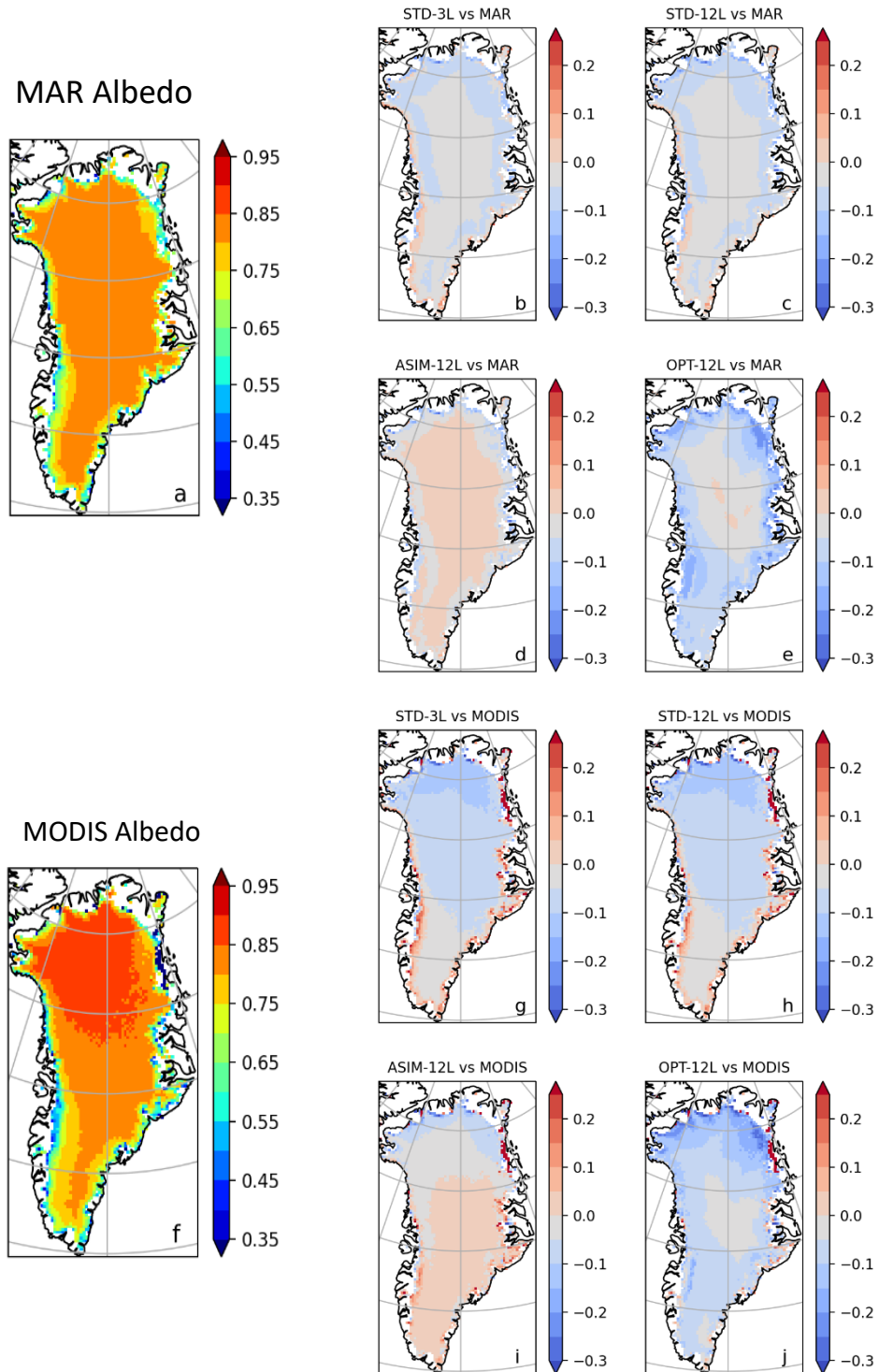
598 **Figure 5:** Spatial distribution of the GrIS SMB simulated with MAR (in  $\text{mm day}^{-1}$ ) and averaged over the 2000-  
 599 2019 period (a) Differences in the GrIS surface mass balance between MAR and the ORCHIDEE-ICE model (b-  
 600 e) with the standard parameter values of the albedo parameterisation and the three-snow layering scheme (b).  
 601 Panels (c-e) correspond to simulations performed with the updated twelve-snow layering scheme for standard  
 602 values of the albedo parameters (c), optimised values of the albedo parameters (d), values of the albedo parameters  
 603 obtained after manual tuning (e).

## 604 5.2. SMB and runoff for modified albedo parameters

### 605 5.2.1 Impact of optimised albedo parameters

606 As snow is a highly reflective medium, little changes in albedo may produce large changes in the surface energy  
 607 balance, and thus, in the SMB. In the GrIS interior, there is generally a quite good agreement between the summer  
 608 albedo computed by MAR and the standard ORCHIDEE-ICE simulations (i.e. STD-3L and STD12-L experiments,  
 609 Figs. 6b and 6c and S5) with slight negative anomalies of less than 0.05. Negative anomalies ( $\sim -0.1$ ) also appear,  
 610 mainly in the northern part of the ice sheet, but with only little consequences on surface melting owing to the very  
 611 cold conditions in this region. However, on the western margin, where most of the melting takes place, larger snow  
 612 albedo values are found in ORCHIDEE-ICE. This leads to underestimated surface temperatures compared to MAR  
 613 (Fig. 7) and, thus, to undervalued runoff that may explain part of the discrepancies between MAR and  
 614 ORCHIDEE-ICE. There are also differences between the observations provided by MODIS retrievals and the  
 615 MAR albedo (Figs. 6a and 6f), especially in the northern and southern parts, and the western margin. On the other  
 616 hand, the summer albedo computed in the STD-3L and STD-12L experiments (Figs. 6g and 6h) are generally too  
 617 low in the interior of the ice sheet, and too high on the western margin with differences from 0.05 to 0.15.

## Summer albedo differences (2000 – 2017)



618

619 **Figure 6:** Left: Spatial distribution of the summer (JJA) albedo computed with MAR (a) and MODIS (f) and  
 620 averaged over the 2000-2017 period. Right: Differences between the albedo computed with ORCHIDEE-ICE and  
 621 MAR (b,c,d,e) and between ORCHIDEE-ICE and MODIS (g,h,i,j) for the three-layer snow scheme and the  
 622 standard albedo parameters (b,g), the twelve-layer snow scheme and the standard albedo parameters (c,h), the  
 623 albedo parameters inferred from a data assimilation technique and using a previous version of the ORCHIDEE-  
 624 ICE model (d,i), the albedo parameters obtained after manual tuning (e,j).

625 As mentioned in Section 3.2, we investigated the sensitivity of the SMB and its components to the albedo. We first  
 626 performed an ORCHIDEE-ICE experiment (ASIM-12L) with the optimised albedo parameters inferred from  
 627 Raoult et al. (2023). Figure 6i illustrates how the representation of the albedo has been improved in the ASIM-12L  
 628 experiment compared to STD-12L (Figs. 6h, S5 and S8). Model-data discrepancies are now reduced with  
 629 differences lower than 0.05 except in the northernmost parts of the ice sheet. The RMSE decreased by ~26% (Table  
 630 3), which is quite consistent with Raoult et al. (2023). The ablation areas are now better represented (Fig. 2d) due  
 631 to increased surface temperatures (Fig. 7c) as a result of lower albedo values on the western margin (Fig. 6i).

632 **Table 3:** Albedo RMSE values (2<sup>nd</sup> column), areal mean biases (3<sup>rd</sup> column) and spatial RMSE with respect to  
 633 MODIS (top) and MAR (bottom).

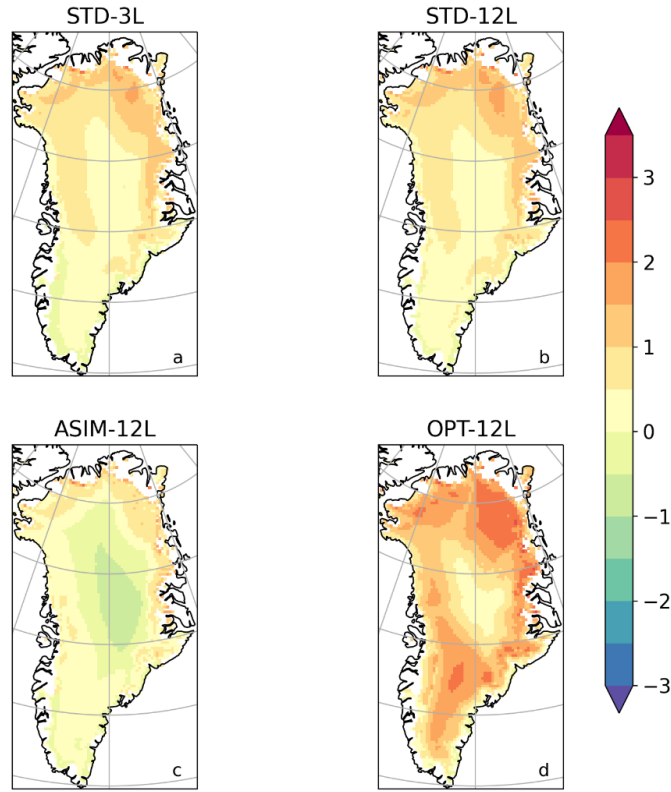
Experiments	RMSE (w.r.t MODIS)	Areal mean bias (w.r.t MODIS)	Spatial RMSE (w.r.t MODIS)
MAR	0.076	- 0.005	
STD-3L	0.098	- 0.047	0.098
STD-12L	0.097	- 0.051	0.097
ASIM-12L	0.072	0.001	0.072
OPT-12L	0.111	- 0.008	0.092
Experiments	RMSE (w.r.t MAR)	Areal mean bias (w.r.t. MAR)	Spatial RMSE (w.r.t MAR)
STD-3L	0.055	- 0.042	0.055
STD-12L	0.058	- 0.047	0.058
ASIM-12L	0.051	0.006	0.040
OPT-12L	0.092	- 0.047	0.092

634  
 635 However, despite the smaller mismatch between modeled ASIM-12L albedo and MODIS retrievals and the better  
 636 representation of the ablation areas, the simulated amount of runoff (217 Gt yr<sup>-1</sup>) integrated over the whole GrIS  
 637 has been only slightly improved with respect to STD-12L (Figs. 2d) and remains quite different from MAR outputs  
 638 (Figs. 2a). In addition, the simulated SMB (466 Gt yr<sup>-1</sup>) has even been slightly degraded (Figs. 5a and 5d) due to  
 639 negative temperature anomalies in central Greenland extending until the southern tip (Fig. 7c) resulting from  
 640 slightly higher albedo values compared to MAR and MODIS (Figs 6a, 6i).

641



## Summer snow surface temperature differences with MAR



642

643 **Figure 7:** Spatial distribution of the snow temperature differences with respect to MAR averaged over the 2000-  
644 2019 period (in °C) simulated for the STD-3L (a), STD-12L (b), ASIM-12L (c) and OPT-12L (d) experiments.

645 The low performance for the SMB computation in ASIM-12L is not solely due to a small amount of runoff but  
646 also to strong negative values of sublimation (i.e. large condensation) over central Greenland (Fig. 3d) resulting  
647 in an average level of - 5 Gt yr<sup>-1</sup> over the entire ice sheet compared to 82 Gt yr<sup>-1</sup> in MAR (Table 2). In the ASIM-  
648 12L experiment, the albedo in the central GrIS region is slightly higher (up to 0.05) than the albedo retrieved from  
649 MODIS (Fig. 6i), while the albedo computed with MAR is slightly lower (Figs. 6a and 6f). This explains why the  
650 ASIM-12L surface temperatures are smaller than those simulated with MAR. This can lead, therefore, to lower  
651 saturation pressures that can drop below the dew point and thus produce solid condensation. This result highlights  
652 the key influence of the albedo on surface processes and, in particular, illustrates how a small departure from  
653 observations may lead to strong biases in sublimation estimates.

### 654 5.2.2 Manual tuning

655 As mentioned in Section 3, we have not yet performed a data assimilation experiment to calibrate the new twelve-  
656 layer ES model, given the computational cost of such an experiment. Instead, we chose to follow a trial-and-error  
657 approach. As runoff dominates the SMB signal, our primary objective was to improve the runoff computation by  
658 reducing the summer albedo values in the main ablation areas (i.e. the western margin). Given the number of  
659 albedo parameters, several options are available to achieve this:

- 660 • lowering the albedo of aged snow ( $A_{aged}$ ) and/or the albedo of fresh snow ( $A_{aged} + B_{dec}$ );
- 661 • modifying the parameter controlling the decay rate of snow albedo ( $\tau_{dec}$ );

- 662 • increasing snow age by changing the parameters related to snow aging: the minimum snowfall thickness  
663 to reset snow age to zero ( $\delta_c$ ), the tuning parameters  $\omega_1$ ,  $\omega_2$  (see Eq. 10) and the maximum snow age  
664 ( $\tau_{max}$ );
- 665 • changing the ice albedo ( $\alpha_{ice}$ ) because it can also affect SMB and runoff computation if the snowpack  
666 melts entirely during summer months in some places and give rise to bare ice.

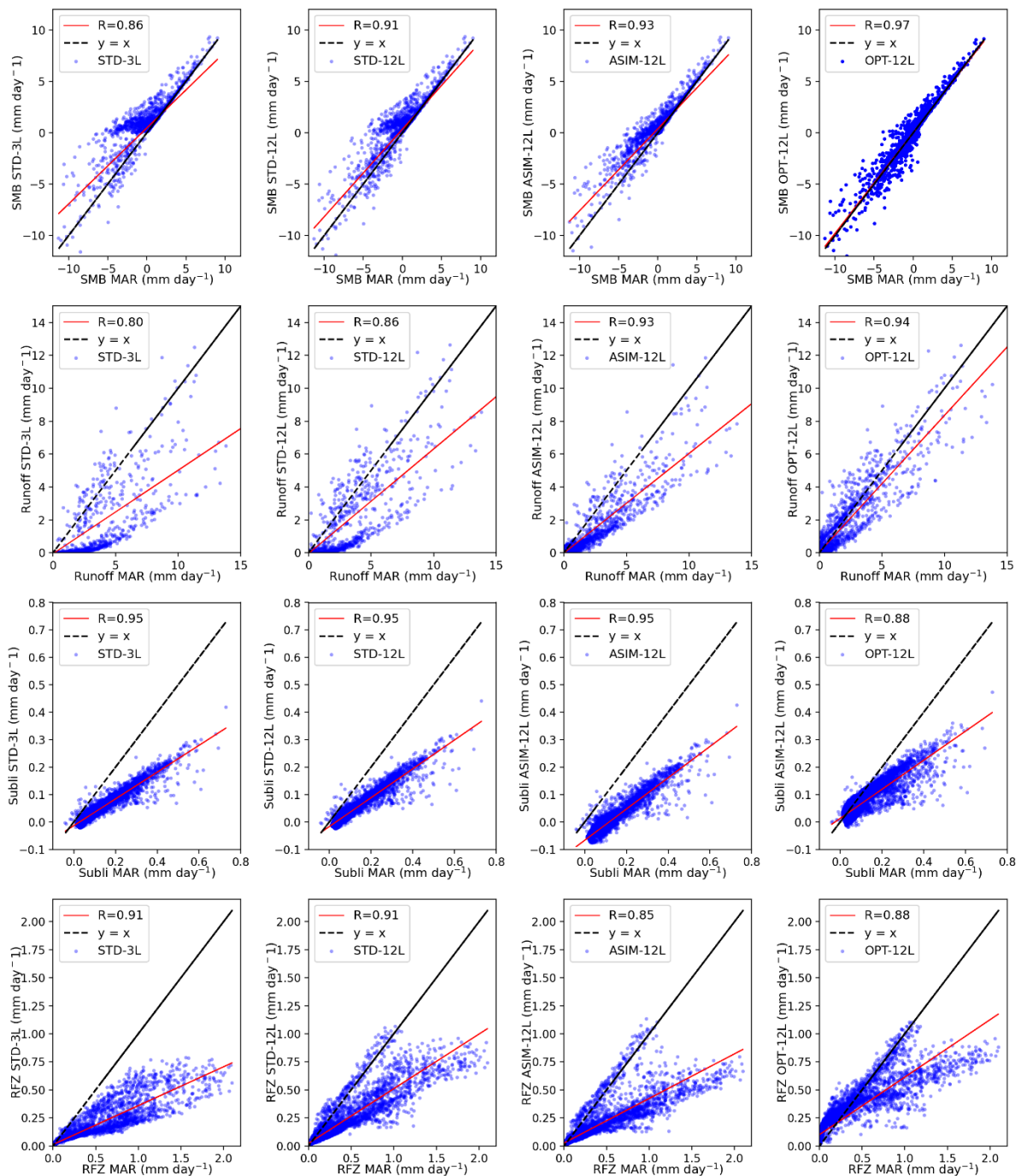
667 Owing to the various influences of the albedo parameters, we had to find a compromise so as to lower the albedo  
668 in ablation areas and improve the computation of runoff and SMB, while keeping reasonable albedo values in the  
669 GrIS interior. Among the values we tested for each of the parameters, the set of parameters providing the best  
670 agreement with MAR outputs (for SMB and SMB components) is highlighted in bold in Table 1 (OPT-12L  
671 experiment). Compared to the ASIM-12L experiment (Figs. 6i, S5, S8), the albedo mismatch between  
672 ORCHIDEE-ICE (OPT-12L experiment) and MODIS is amplified, especially along the western margin and in the  
673 northern sector with differences reaching 0.25 and 0.3 respectively (Fig. 6j). Nevertheless, these results were  
674 expected since our manual tuning was designed to increase the magnitude of the ablation components (especially  
675 runoff) and to decrease the SMB, and therefore to lower the albedo values with a direct impact on surface  
676 temperatures, hence surface melting and sublimation.

### 677 5.2.3 Impact on SMB components

678 Using the new set of albedo parameters obtained with the manual tuning approach, the ablation areas are now  
679 much more extended than those simulated in the STD-12L experiment (Figs. 2c and 2e). Compared to MAR (Fig.  
680 2a), they are even wider in the northern part due to increased surface temperatures (Fig. 7d) in response to lower  
681 albedo values (up to -0.25). The total amount of runoff averaged over the 2000-2019 period is now 336 Gt yr<sup>-1</sup>  
682 (against 375 Gt yr<sup>-1</sup> in MAR). For the OPT-12L experiment, the RMSE value decreased by ~40% compared to  
683 STD-12L (Table 2). In the same way, the sublimation (52 Gt yr<sup>-1</sup>) and refreezing (158 Gt yr<sup>-1</sup>) better match with  
684 MAR (Table 2). In particular, condensation over central Greenland has been considerably reduced, notably with  
685 respect to ASIM-12L, but sublimation is still underestimated along the GrIS edges and in the southern part (Fig.  
686 4e). The increase in refreezing (with respect to STD-12L and ASIM-12L) in the GrIS interior (Fig. 3e) is likely  
687 linked to lower summer albedo values (Figs. 6e and 6j) leading to a smaller amount of melting compensated by  
688 refreezing. In the main ablation areas, a larger refreezing is produced and thus a better agreement with MAR,  
689 though still insufficient, is obtained.

690 These results for the SMB components are evidently associated with an improved representation of the SMB itself  
691 (Fig. 5e) which now reaches 301 Gt yr<sup>-1</sup> (286 Gt yr<sup>-1</sup> obtained with MAR). Indeed, the RMSE and the spatial RMSE  
692 values have been reduced by ~41% and 10% respectively for the SMB (~28% and 9% for the runoff) compared to  
693 the STD-12L experiment (Table 2). An even more striking result concerns the areal mean bias which has been  
694 lowered by one order of magnitude. These improvements are also illustrated in Figure 8, which displays the  
695 monthly mean values for each grid point of the SMB components simulated with ORCHIDEE-ICE as a function  
696 of the same MAR variables (see for example the correlation coefficient for both SMB and runoff for the OPT-12L  
697 experiment). However, our results are less conclusive for sublimation and refreezing. Although, the areal-mean  
698 bias and the RMSE values indicate a better match between the OPT-12L and the MAR simulations, the spatial  
699 RMSE values are greater compared to the three other ORCHIDEE-ICE experiments, suggesting a lower temporal  
700 consistency between OPT-12L and MAR. In addition, the correlation coefficients for sublimation and refreezing

701 are also smaller (Fig. 8). On the other hand, the best overlaps between the probability density functions between  
 702 MAR and the ORCHIDEE-ICE experiments is undoubtedly obtained for OPT-12L, as shown in Figs. S6-S7 and  
 703 the scores of the CVM tests reported in Table S1.



704  
 705 **Figure 8:** Representation of the simulated SMB (1<sup>st</sup> row), runoff (2<sup>nd</sup> row), sublimation (3<sup>rd</sup> row) and refreezing  
 706 (4<sup>th</sup> row) simulated with ORCHIDEE-ICE as a function of the same MAR variables: STD-3L (1<sup>st</sup> column), STD-  
 707 12L (2<sup>nd</sup> column), ASIM-12L (3<sup>rd</sup> column) and OPT-12L (4<sup>th</sup> column). The different points represent the monthly  
 708 mean values over the period 2000-2019 for each of the grid points. The regression line is displayed in red (R is the  
 709 regression coefficient) and the line  $y = x$  is in black.

710 Despite these encouraging results, it is important to underline that the improved SMB simulation in OPT-12L is  
711 achieved through the albedo reduction, and therefore, to some extent, come from error compensation. However,  
712 the reduced albedo also makes it possible to compensate for the effect of some missing mechanisms, such as the  
713 lack of consideration of snow-atmosphere interactions or the absence of an explicit representation of snow  
714 metamorphism, which has a direct impact on the density profile, the albedo itself and the temperature profile.

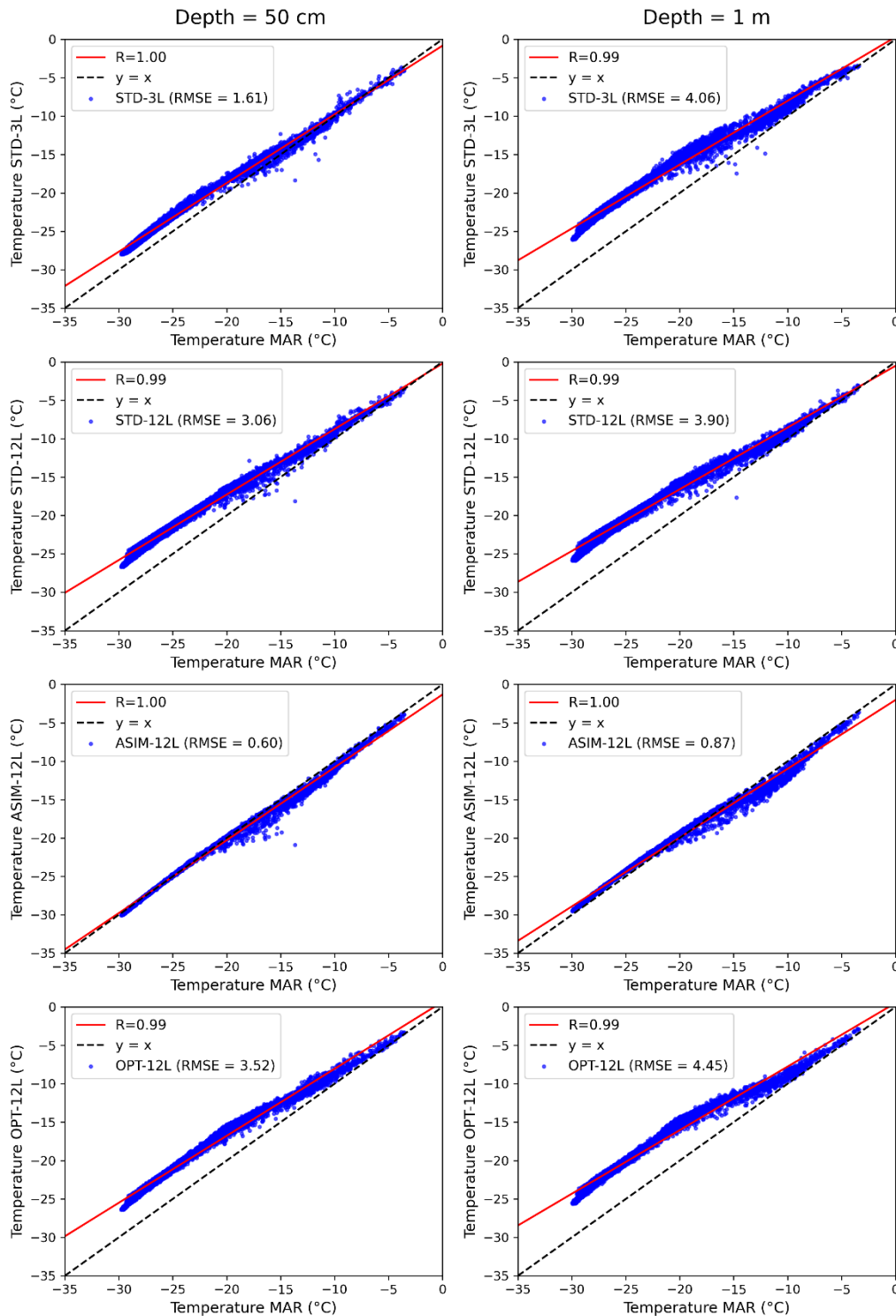
### 715 **5.3 Vertical temperature and density profiles**

716 To go a step further and gain a better understanding of the above results, it is also important to explore the internal  
717 processes of the snowpack. To achieve this, we chose to focus on the vertical temperature and density profiles.  
718 Figure 9 depicts the snow temperatures simulated ORCHIDEE-ICE as a function of the MAR snow temperatures  
719 at 20 cm and 1 m depth of the snowpack. These plots show that the temperatures simulated in STD-3L, STD-12L  
720 and OPT-12L behave approximately in the same way when compared to those of MAR. In the first 20 cm,  
721 ORCHIDEE-ICE is slightly warmer than MAR for temperatures between  $-30^{\circ}\text{C}$  and  $-10^{\circ}\text{C}$ , despite a few slightly  
722 colder grid points appearing in the range of  $-20^{\circ}\text{C}$  to  $-10^{\circ}\text{C}$ . The ASIM-12L experiment presents the best agreement  
723 with MAR, although slightly lower temperatures. These features reflect directly the behavior of surface  
724 temperatures (Fig. 7) that strongly influence the upper snowpack layers. Another key point arising from these plots  
725 is the very good agreement between MAR and ORCHIDEE-ICE for temperatures above  $-10^{\circ}\text{C}$ . This suggests that  
726 the potential runoff that could occur in the first tens of centimeters of the snowpack should not be so much affected.  
727 However, the departure from MAR increases with snow depth, especially for low temperatures. For example, at  
728 1 m depth, differences of  $3\text{-}4^{\circ}\text{C}$  are obtained (Fig. 9) and may exceed  $5^{\circ}\text{C}$  for deeper levels (not shown). These  
729 enhanced differences with MAR are likely due to a positive feedback related to the thermal conductivity (see Eq.  
730 33): As snow temperature increases by  $1^{\circ}\text{C}$  in a given layer, the thermal conductivity increases by one order of  
731 magnitude.

732 As pointed out by Domine et al. (2019), the snow thermal regime and snow density are strongly coupled. As an  
733 example, they mentioned the work of Fréville (2015) who showed that an error of  $1^{\circ}\text{C}$  in the surface temperature  
734 can lead to errors on snow density of  $100\text{ kg m}^{-3}$ . Our experiments show that for a depth of 20 cm, the higher the  
735 surface temperature, the lower the snow density on average (Fig. 10). On the other hand, in the ASIM-12L  
736 experiment, snow temperatures are lower, compared to the three other ORCHIDEE-ICE experiments, and snow  
737 densities are larger. This contradicts a number of studies (e.g. Kojima, 1967; Anderson 1976, Mizukami and Perica,  
738 2008), which have shown that in a warmer snowpack, snow grains become rounded and are more prone to be  
739 compacted more easily, hence leading to an increase in snow density. However, in our model this process cannot  
740 be reproduced as snow metamorphism is only accounted for through snow ageing. Conversely, in deeper layers,  
741 the model is more effective at densifying (Fig. 10), in line with the fact that warmer snow becomes more plastic  
742 and compacts more easily. In particular; between 20 cm and 1 m depth, the RMSE computed between OPT-12L  
743 and MAR has been reduced from  $79.63\text{ kg m}^{-3}$  to  $30.22\text{ kg m}^{-3}$ . Beyond  $600\text{ kg m}^{-3}$ ; the ORCHIDEE-ICE densities  
744 are generally below those of MAR because the maximum density is fixed to  $750\text{ kg m}^{-3}$  (see Section 2). However,  
745 the comparison of our results on snow density with those of MAR should be viewed with caution because, to the  
746 best of our knowledge, the snow density simulated by MAR has not been evaluated against available observations.

747

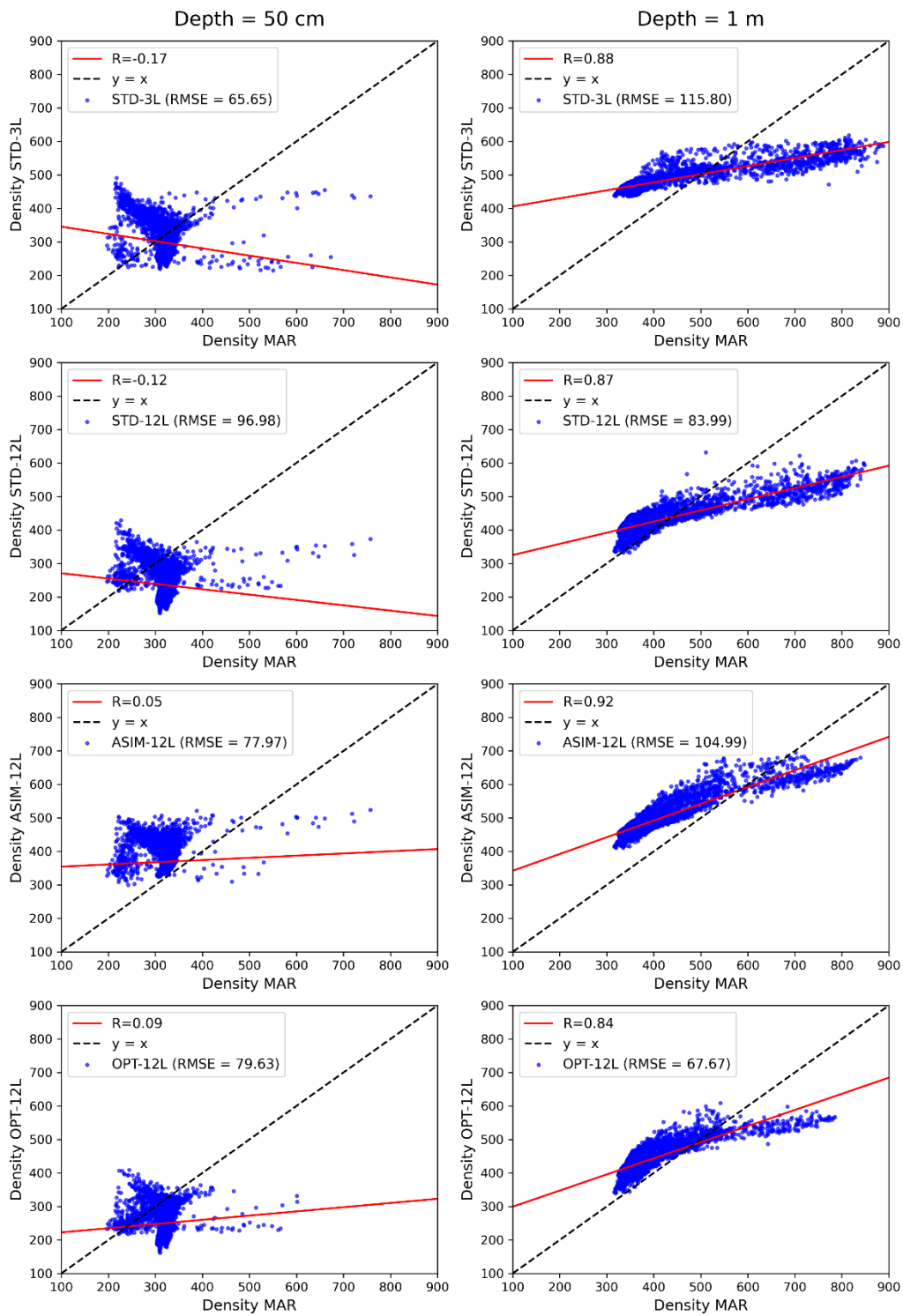
## Snow Temperature 2000-2019 (°C)



748

749 **Figure 9:** Representation of the ORCHIDEE-ICE simulated snow temperatures at 50 cm (left) and one-meter  
 750 depth (right) as a function of the MAR snow temperatures. The different points represent the monthly mean values  
 751 over the period 2000-2019 for each grid point. The regression line is displayed in red (R is the regression  
 752 coefficient) and the line  $y = x$  is in black.

Snow Density 2000-2019 ( $\text{kg m}^{-3}$ )



754

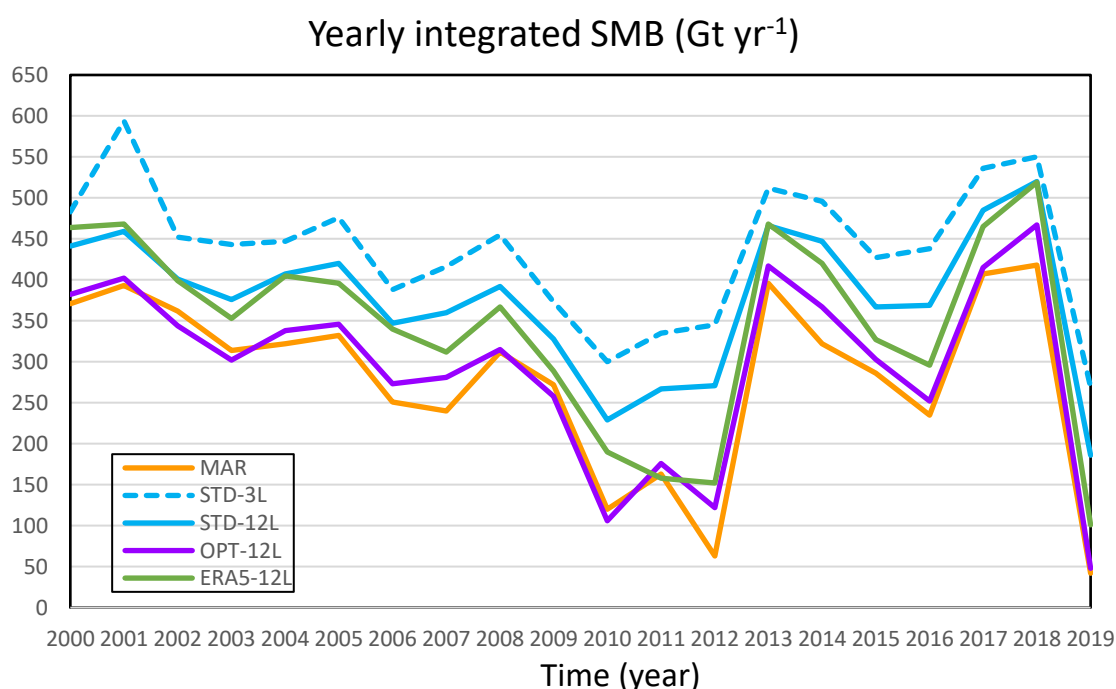
755 **Figure 10:** Same as Figure 9 for snow density

756

757

758 **5.4 SMB evolution: impact of the climate forcing**

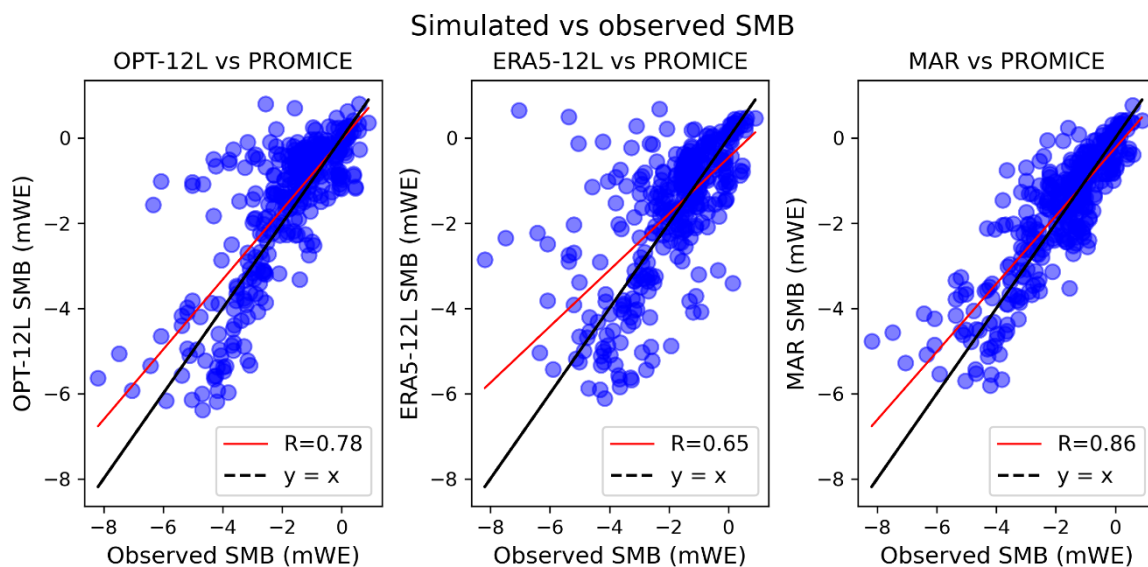
759 The results presented in the previous sections were averaged over the 2000-2019 period (for SMB and the SMB  
760 components) and over the 2000-2017 period (for the albedo). In this part, we present the temporal evolution of the  
761 SMB between the years 2000 and 2019 (Fig. 11). Figure 11 shows that whatever the ORCHIDEE-ICE experiment  
762 under consideration, the evolution of the yearly integrated SMB is in accordance with the evolution simulated by  
763 the MAR model. In particular, the years in which extreme melting events were recorded (such as 2012 and 2019)  
764 are perfectly well represented (Bennartz et al. 2013; Tedesco and Fettweis 2020). As expected, the best agreement  
765 with MAR is obtained for the OPT-12L experiment as a result of the calibration of the albedo parameters.  
766 When forced by the ERA-5 meteorological fields, and using the manually-tuned parameters, ORCHIDEE-ICE  
767 simulates higher SMB values and a lower runoff (Fig. 11 and Table 2), especially during the first period of the  
768 time series (2000-2008). However, the evolution of the yearly integrated SMB in the ERA5-12L experiment  
769 follows exactly the same interannual variations as for the OPT-12L experiment forced with MAR (Fig. 11). This  
770 indicates that the surface climate simulated by MAR is close to that derived from the ERA-5 products. Moreover,  
771 in a comparative study of the ERA-5 reanalyses, Arctic System reanalysis and MAR performances, Delhasse et  
772 al. (2020) showed that MAR outperforms ERA-5 for the near-surface temperatures when compared to observations  
773 from automatic weather stations. As the surface melt, and thus the SMB, largely depend on near-surface  
774 temperatures, there is, therefore, a strong interest in using MAR to force our snow model and to compare its  
775 performances to those of MAR.  
776



777  
778 **Figure 11:** Evolution of the yearly surface mass balance of the Greenland ice sheet simulated with MAR (black),  
779 ORCHIDEE-ICE forced by MAR outputs (STD-3L and STD-12L: yellow, solid and dashed lines respectively;  
780 OPT-12L: red line), ORCHIDEE-ICE forced by the ERA-5 reanalyses (green line).



781 In this paper, we have so far limited the comparison of our results to those of MAR. However, as mentioned in  
 782 Section 4, we also evaluated the simulated SMB with 353 daily SMB observations from the PROMICE database  
 783 available over the 2000-2019 period (Machguth et al., 2016; Mankoff et al., 2021). In addition, it is also interesting  
 784 to evaluate our model results against observations when ORCHIDEE-ICE is forced by climatic fields independent  
 785 from MAR outputs. To address this issue, we plotted the modelled SMB for OPT-12L, ERA5-12L and MAR for  
 786 the grid points located closest to the observation sites as a function of the PROMICE SMB measurements (Fig. 12).  
 787 We also provided statistical elements for the comparison between MAR, the five ORCHIDEE-ICE  
 788 experiments and the SMB observations (Table 4). This model-data comparison confirms the conclusions we  
 789 reached when evaluating the performance of our model against MAR outputs, namely the significant improvement  
 790 in our results when moving from STD-3L to OPT-12L. Moreover, although the bias between the OPT-12L SMB  
 791 and the observed SMB is twice as high as for MAR, the model-data correlation is of the same order of magnitude  
 792 as for MAR (Table 4).  
 793



794  
 795 **Figure 12:** Simulated SMB in the OPT-12L experiment and in MAR as a function of the observed SMB from the  
 796 PROMICE network. As the observed SMB values are not all available over the same time interval, the  
 797 measurements are given in meter water equivalent (mWE). 353 observations were available over the 2000-2019  
 798 period. Each simulated SMB value corresponds to the grid points located closest to the observation sites. The red  
 799 line is the regression line with R being the correlation coefficient and the dashed black line indicates the line  $y =$   
 800  $x$ .

801 The ERA5-12L experiment also produces a good agreement with the observations. Despite a lower correlation  
 802 coefficient than for MAR and OPT-12L, the mean bias is of the same order of magnitude as that of MAR and the  
 803 RMSE on the SMB obtained is the lowest for any of the experiments. It is clear that the SMB simulated in the  
 804 experiments forced by MAR is partly driven by the climate simulated by MAR itself (for the accumulation  
 805 component). However, the results obtained with ERA5-12L clearly show that the behaviour of our model is  
 806 consistent whatever the climate forcing used. Nevertheless, it should be reminded that the resolution of  
 807 ORCHIDEE-ICE corresponds to that of the model used as a forcing. For ERA5-12L, the resolution is about twice



808 as fine as for the experiments forced by MAR (20 km x 20 km). Thus, to make our comparison between ERA5-  
 809 12L, MAR and/or OPT-12L more robust, we should have used MAR with a resolution of 10 km x 10 km. It cannot  
 810 therefore be ruled out that the results for OPT-12L would then have provided a better comparison with the  
 811 PROMICE data than ERA5-12L.

812 **Table 4:** Comparison of the simulated SMB in MAR, STD-3L, STD-12L, ASIM-12L and OPT-12L with the  
 813 SMB observations from the PROMICE network. The bias is computed as the average between modelled and  
 814 observed SMB for each grid point. Note that the values of the bias and the RMSE are given in mWE as the observed  
 815 SMB values are not all available over the same time interval.

Experiments	Bias (mWE)	Correlation	RMSE (mWE)
MAR	0.14	0.86	0.82
STD-3L	0.94	0.67	1.70
STD-12L	0.68	0.73	1.43
ASIM-12L	0.74	0.75	1.33
OPT-12L	0.30	0.78	1.13
ERA5-12L	0.17	0.65	1.07

## 816 6. Discussion and concluding remarks

817 The land surface component of the IPSL ESM used for CMIP6 included a three-layer snowpack model operating  
 818 over continental surfaces. However, this snow scheme was not adapted to glaciated surfaces, which is a major  
 819 drawback and makes it impossible to compute the surface mass balance over ice sheets or glaciers. The aim of this  
 820 paper was therefore to present the new developments made to adapt the snow model to ice-covered areas and to  
 821 document its performance. Our first step was to calibrate the snow albedo parameterisation over the Greenland ice  
 822 sheet. To have a set of climate variables covering the whole ice sheet, we chose to force our model by the  
 823 atmospheric outputs of the MAR regional model which shows very good performances to simulate the surface  
 824 climate and thus offers undeniable advantages for the representation of the physical processes related to snow and  
 825 ice, in particular surface melting (Delhasse et al., 2020). We have shown that the ablation-related processes are  
 826 highly dependent on the choice of the albedo parameters. The set of parameters obtained after manual tuning (OPT-  
 827 12L experiment) provides a good agreement between the SMB computed in ORCHIDEE-ICE and MAR.  
 828 However, as outlined in Section 5.2.3, this improvement is mainly the result of albedo lowering. The summer  
 829 albedo computed with this set of parameters has been degraded compared to MAR and MODIS and to the albedo  
 830 computed in the ASIM-12L experiment (based on the MODIS-optimised albedo parameters) as shown in Table 3  
 831 and in Figures 6i-6j and S5, S8. While the RMSEs computed between ORCHIDEE-ICE and MAR for SMB and  
 832 runoff have been reduced by ~39% and ~33% respectively from ASIM-12L to OPT-12L, the RMSE for albedo  
 833 has increased by 47% (Table 3). The mismatch between MODIS retrievals and OPT-12L albedo is mainly observed  
 834 in the northernmost part of the ice sheet and, to a lesser extent, on the western edge.

835 A more objective method would have been to perform a data assimilation experiment similar to the one presented  
836 in Raoult et al. (2023) using the new version of the ORCHIDEE-ICE model. However, albedo is not the only  
837 important parameter governing the snowpack evolution. The albedo parameters inferred from Raoult et al. (2023)'s  
838 optimisation greatly improve the representation of the albedo, but degrade the other model outputs compared to  
839 those obtained with the manually-tuned albedo parameters. This is most likely because their optimisation overfits  
840 the albedo retrievals without applying constraints to the other processes strongly impacting the SMB components  
841 and controlling the state of the snowpack (e.g. snow compaction, snow density, snow viscosity). This supports the  
842 recommendation for a multi-objective optimisation using not only albedo data, but also vertical temperature and  
843 density profiles as well as SMB observations. Since this type of approach is highly time-consuming, it has not yet  
844 been undertaken but could be the objective of a future study.

845 However, the reduction in albedo in the current ORCHIDEE-ICE version can compensate for missing processes.  
846 For example, snow drift, transmission of solar radiation, or the effect of light absorbing particles on the albedo are  
847 ignored. Metamorphism is not explicitly represented although its effect on the albedo and the vertical density  
848 profile are accounted for (albeit in a crude manner) through the snow ageing function  $f_{age}$  (Eq. 7) and the  $\psi_{snow}$   
849 function (Eq. 17) respectively.

850 In the GrIS, snow erosion has often been considered as a second-order component of mass loss in ablation areas  
851 compared to melt water. However, in the ice sheet interior, sublimation and snow erosion are dominant processes  
852 in removing mass from the surface, and may have, therefore, a significant impact on SMB (van Angelen et al.,  
853 2011).

854 Taking into account the transmission of solar radiation within the snowpack can lead to a warming of the internal  
855 layers, with higher temperatures near the surface and lower temperatures at depth due to the exponential decrease  
856 in heat transfer. This results in a temperature gradient that influences the metamorphism of snow grains and thus  
857 accelerates densification (Colbeck, 1983). We showed that the ORCHIDEE-ICE temperatures inside the snowpack  
858 were higher than those simulated by the MAR model. A likely hypothesis to explain this behaviour relies on the  
859 reduction in albedo, which leads to excessively high surface temperatures. However, it is important to note that  
860 heat transfer can promote snow melting, which in turn can percolate at depth and refreeze, affecting both the runoff  
861 and the vertical structure of the snowpack through changes in density (Colbeck, 1983). Quantifying all these  
862 processes requires, therefore, the proper representation of solar absorption, which is itself strongly dependent on  
863 snow optical properties (Warren, 1982) and, therefore, on snow grain size (Libois et al., 2013). Since  
864 metamorphism is not explicitly represented in the model, we assumed that representing solar absorption was not a  
865 priority in our modeling approach, even if this choice is debatable. However, in the near future, a more  
866 sophisticated albedo scheme based on a transfer radiative model accounting for light-absorbing particles and snow  
867 grain size (Kokhannovsky and Zege, 2004) will be implemented in the ORCHIDEE-ICE model. This will allow  
868 to represent the backward and forward scattering processes as well as light absorption.

869 In addition, there are also structural deficiencies related to the fact that in ORCHIDEE-ICE, a single energy balance  
870 is computed in one grid cell. This is detrimental for the albedo computation especially at the edges of the ice sheet  
871 where several surface types may coexist in a 20 km x 20 km mesh. However, the implementation of a multi-tile  
872 energy balance is currently under development.

873 Finally, as our simulations have been run in off-line mode, the snow feedback onto the atmosphere has not been  
874 taken into account, contrary to the MAR model fully coupled to a snow scheme derived from CROCUS (Brun,

875 1989, 1992). Ignoring snow-atmosphere feedback may potentially lead to biases related to surface processes and  
876 to an improper representation of the energy and humidity flux exchanges at the snow-atmosphere interface. For  
877 example, forcing our model with the atmospheric temperature at 2m derived from the full coupled MAR simulation  
878 could lead to an underestimation of the energy available at the snow-atmosphere interface, resulting in less  
879 snowmelt compared to what is simulated in coupled mode. However, our manual tuning approach aims at limiting  
880 the potential underestimation of the surface meltwater production. Conversely, any potential bias in the MAR  
881 forcing may also affect our results (Dietrich et al., 2024). To overcome this problem, it would have been interesting  
882 to force ORCHIDEE-ICE by meteorological fields recorded at the automatic weather stations. This has not been  
883 done in this study because the meteorological fields required to force ORCHIDEE-ICE were not all available at  
884 the PROMICE stations and because our first objective was to obtain a reasonable estimate of the SMB and its  
885 components at the scale of the entire GrIS.

886 Despite the potential improvements that could still be made to ORCHIDEE-ICE to enhance the model's  
887 performance, the developments presented in this paper represent a major step forward. Indeed, they now allow the  
888 ice-sheet surfaces to be handled by the land surface model, consistently with all the other surface types, and not  
889 by the atmospheric component of the IPSL model (LMDZ), as was the case up to now. In addition, the new snow  
890 model can now be applied to the continental glaciers replacing the very crude snow scheme used previously. Our  
891 developments enable us to provide a reasonable estimate of the surface mass balance of the Greenland ice sheet,  
892 in very good agreement with that simulated by the MAR model which was used as a reference in this study. These  
893 developments constitute a first step towards the full coupling between the IPSL global climate model and ice-sheet  
894 models.

895

Symbol	Variable	Units	Value/Range
$\alpha$	Surface albedo of the grid cell		
$\alpha_{snow}$	Albedo of a snow-covered surface		
$\alpha_{snow-free}$	Albedo of snow-free surface		
$\alpha_{ice}$	Ice albedo		
$\delta_c$	Snowfall thickness necessary for resetting the snow age to zero	$\text{kg m}^{-2} \text{s}^{-1}$	
$\eta_{snow}$	Snow viscosity	Pa s	
$\eta_0$	Snow viscosity parameter	Pa s	$3.7 \times 10^7$
$\Lambda_{snow} (\Lambda_{ice})$	Snow (ice) thermal conductivity	$\text{W m}^{-1} \text{K}^{-1}$	
$\Lambda_{eff} = \Lambda_{snow}$	Effective snow thermal conductivity	$\text{W m}^{-1} \text{K}^{-1}$	
$\Lambda_{cond}$	Snow thermal conductivity	$\text{W m}^{-1} \text{K}^{-1}$	
$\Lambda_{vap}$	Snow thermal conductivity	$\text{W m}^{-1} \text{K}^{-1}$	
$\lambda_{snow}$	Integration coefficient for snow thermal profile numerical scheme		
$\lambda_{ice}$	Integration coefficient for ice thermal profile numerical scheme		
$\rho_{snow}$	Snow density	$\text{kg m}^{-3}$	917
$\rho_{ice}$	Ice density	$\text{kg m}^{-3}$	
$\rho_{water}$	Water density	$\text{kg m}^{-3}$	1000
$\rho_{air}$	Air density	$\text{kg m}^{-3}$	
$\rho_t$	Parameter of the maximum water holding capacity	$\text{kg m}^{-3}$	200
$\rho_\psi$	Parameter for the effect of metamorphism in the snow density	$\text{kg m}^{-3}$	150
$\sigma_{snow}^i$	Pressure of the snow load over the $i^{\text{th}}$ layer	Pa	
$\tau_{snow}$	Snow age	days	
$\tau_{dec}$	Time constant of the albedo decay	days	
$\tau_{max}$	Maximum snow age	days	
$\omega_1, \omega_2$	Tuning constants for snow albedo		
$A_{aged}$	Snow albedo of old snow		

$A_i$	Surface area of the $i^{th}$ grid point	$m^2$	
$a_\eta$	Snow viscosity parameter	$K^{-1}$	$8.1 \times 10^{-2}$
$a_\psi$	Parameter for the effect of metamorphism	$s^{-1}$	$2.8 \times 10^{-6}$
$a_\lambda$	Parameter for snow thermal conductivity	$W m^{-1} K^{-1}$	0.02
$a_{\lambda v}$	Parameter of snow thermal conductivity from vapor transport	$W m^{-1} K^{-1}$	-0.06023
$a_{ci}$	Parameter of heat capacity of the ice	$J K^{-1} kg^{-1}$	2115.3
$a_{\lambda i}$	Parameter of ice thermal conductivity	$W m^{-1} K^{-1}$	6.627
$B_{dec}$	Decay rate of snow albedo		
$b_\eta$	Snow viscosity parameter	$m^3 kg^{-1}$	$1.8 \times 10^{-2}$
$b_\psi$	Parameter for the effect of metamorphism	$K^{-1}$	$4.2 \times 10^{-2}$
$b_\lambda$	Parameter of snow thermal conductivity	$W m^5 K^{-1} kg^{-2}$	$2.5 \times 10^{-6}$
$b_{\lambda v}$	Parameter of snow thermal conductivity from vapor transport	$W m^{-1}$	-2.5425
$b_{ci}$	Parameter of heat capacity of the ice	$J K^{-2} kg^{-1}$	7.79293
$b_{\lambda i}$	Parameter of ice thermal conductivity	$K^{-1}$	-0.041
$c_\psi$	Parameter for the effect of metamorphism	$m^3 kg^{-1}$	$460 m^3 kg^{-1}$
$c_{\lambda v}$	Parameter of snow thermal conductivity from vapor transport	$K$	-289.99
$C_{soil}$	Surface heat capacity of soil	$J m^{-2} K^{-1}$	
$C_{snow}$	Snow heat capacity	$J m^{-2} K^{-1}$	
$C_{snow}^v, (C_{ice}^v)$	Snow (ice) volumetric heat capacity	$J m^{-3} K^{-1}$	
$C_{gr\_snow}, D_{gr\_snow}$	Integration coefficients for snow thermal profile numerical scheme		
$C_{gr\_ice}, D_{gr\_ice}$	Integration coefficients for ice thermal profile numerical scheme		
$D_{snow}^i$	Depth of the $i^{th}$ snow layer	$m$	
$D_{lwe}^i$	Snow water equivalent in the $i^{th}$ snow layer	$m$	
$D_{ice}^i$	Depth of the $i^{th}$ ice layer	$m$	
$dt$	ORCHIDEE time step	$s$	1800
$E_{snow}^i, (E_{ice}^i)$	Energy available to induce phase changes in the snowpack (in the ice)	$W m^{-2} s^{-1}$	
$F_C$	Heat conductive flux	$W m^{-2}$	

$f_{age}$	Snow age function		
$G_{snow}$	Surface energy flux over snow-covered areas	$W m^{-2}$	
$G_{surf}$	Surface energy flux	$W m^{-2}$	
$H$	Sensible heat flux	$W m^{-2}$	
$H_{snow}^i$	Heat content in the $i^{th}$ snow layer	$W m^{-2} s^{-1}$	
$H_{rainfall}$	Heat release from rainfall	$W m^{-2}$	
$LE$	Latent heat flux	$W m^{-2}$	
$L_s$	Latent heat of sublimation	$J kg^{-1}$	$2.8345 \cdot 10^6$
$L_f$	Latent heat of fusion	$J kg^{-1}$	333.7
$LW_{net}$	Net longwave radiation	$W m^{-2}$	
$M_{snow} (M_{ice})$	Total amount of snow (ice) melt at each time step	$kg m^{-2} s^{-1}$	
$N$	Number of unmasked grid points over the entire Greenland ice-covered area		
$N_t$	Number of daily time steps over the years 2000-2019		
$P$	Atmospheric pressure	hPa	
$P_0$	Reference pressure	hPa	1000
$P_{snow}$	Snowfall amount during the time step $dt$	$kg m^{-2} s^{-1}$	
$P_{rain}$	Rainfall amount during the time step $dt$	$kg m^{-2} s^{-1}$	
$Q_{air}$	Air specific humidity at 2 m	-	
$Q_{sat}$	Saturated specific humidity at 2 m	-	
$q_{cdrag}$	Transfer coefficient	-	
$r_{min}$	Parameter of the maximum water holding capacity		0.03
$r_{max}$	Parameter of the maximum water holding capacity		0.10
$SCF$	Snow cover fraction	-	
$S_{snow}$	Snow sublimation	$kg m^{-2} s^{-1}$	
$SMB$	Surface mass balance	$kg m^{-2} s^{-1}$	
$SW_{net}$	Net shortwave radiation	$W m^{-2}$	
$T_{air}$	Surface air temperature at 2 m	K	
$T_{soil}$	Surface temperature	K	

$T_0$	Freezing temperature	K	273.15
$T_{snow}^{add}$	Snow temperature adjustment	K	
$T_{snow}(T_{ice})$	Snow (ice) temperature	K	
$U$	Wind speed at 10 m	$m s^{-1}$	
$W_{liq}^i$	Liquid content in the $i^{th}$ snow layer	m	
$W_{max}^i$	Maximum water holding capacity of the $i^{th}$ snow layer	m	

898

899 **Code availability:** The source code for the ORCHIDEE-ICE version used in this study is freely available online  
900 via the following address <https://doi.org/10.14768/d82899b4-09b4-4337-abb1-75886602fe72> (IPSL Data  
901 Catalogue, 2024). The ORCHIDEE model code is written in Fortran 90 and is maintained and developed under a  
902 subversion (SVN) control system at the Institut Pierre Simon Laplace (IPSL) in France.

903 **Data availability:** The MAR outputs are available at <ftp://ftp.climato.be/fettweis> (last access 30 October 2020).  
904 The MODIS Greenland albedo retrievals MOD10A1 are available at <https://doi.org/10.22008/FK2/6JAQPK> (last  
905 access 22 January 2024, Box et al., 2022). The surface mass balance observations from the PROMICE network  
906 are available at <https://dataverse.geus.dk/dataverse/PROMICE> (last access 06/10/2024, Machguth et al., 2016;  
907 Mankoff et al., 2021).

908 **Author contributions:** SC conceived the project funding the study. SC, CD, FM and CO co-designed the research  
909 and contributed to the code developments. SC and CD performed the preliminary tests with strong support from  
910 FM and CO. CD implemented the new snow-layering scheme and the new icy soil type. XF ran the MARv3.11.4  
911 simulations, provided the MAR outputs and performed the comparison between the simulated SMB and the  
912 PROMICE dataset. NR provided the albedo parameters obtained from the data assimilation experiment. SC, CD,  
913 FM and CO analysed the results with contributions from NR and XF. SC wrote the original draft, with  
914 contributions from CD, FM and CO, and generated the figures. SC and PC analysed the vertical temperature and  
915 density profiles. All co-authors provided comments on the manuscript.

916 **Competing interests:** The authors declare that one of the co-authors is a member of the editorial board of *The*  
917 *Cryosphere*.

918 **Acknowledgements:** This study has received funding from Agence Nationale de la Recherche - France 2030 as  
919 part of the PEPR TRACCS programme under grant numbers ANR-22-EXTR-0010 and ANR-22-EXTR-0008. The  
920 work has also been supported by the French INSU/LEFE OSCAR project. The authors would like to thank all  
921 members of the SNOW working group gathering members from the Institut Pierre Simon Laplace (IPSL, France)  
922 and the Institut des Géosciences de l'Environnement (IGE, France) for numerous and fruitful discussions. They  
923 also thank J.-Y. Peterschmitt for technical support and the core ORCHIDEE team for maintaining the model and  
924 especially J. Ghattas for helping merge the ORCHIDEE-ICE code into the trunk version of the model. Data from  
925 the Programme for Monitoring of the Greenland Ice Sheet (PROMICE) are provided by the Geological Survey of  
926 Denmark and Greenland (GEUS) at <http://www.promice.dk>. They include sites financially supported by the  
927 Glaciobasis programme as part of Greenland Ecosystem Monitoring (<https://g-e-m.dk/>), maintained by GEUS  
928 (ZAK, LYN) and by Asiaq Greenland Survey (NUK\_K). The WEG stations are paid for and maintained by the  
929 University of Graz. The authors are very grateful to two anonymous reviewers who provided insightful comments  
930 that greatly help to improve the manuscript, and to the editor Marie Dumont.

931

933 **References**

- 934 Alexander, P. M., Tedesco, M., Fettweis, X., van de Wal, R. S. W., Smeets, C. J. P. P., and van den Broeke, M.  
 935 R.: Assessing spatio-temporal variability and trends in modelled and measured Greenland Ice Sheet albedo  
 936 (2000–2013), *The Cryosphere*, 8, 2293–2312, doi: org/10.5194/tc-8-2293-2014, 2014.
- 937 Armstrong, R. L. and Brun, E.: *Snow and Climate: Physical processes, surface energy exchange and modeling*,  
 938 Cambridge University Press, 222p., 2008.
- 939 Anderson, E. A.: A point energy and mass balance model of a snow cover, Technical Report NWS 19, National  
 940 Oceanic and Atmospheric Administration (NOAA), Silver Spring, MD, USA, 150pp., 1976.
- 941 Anderson, T. W.: On the distribution of the two-sample Cramer von Mises criterion, *The Annals of Mathematical*  
 942 *Statistics*, 33, 1148–1159, 1962.
- 943 Bakker, P., Schmittner, A., Lenaerts, J. T. M., Abe-Ouchi, A., Bi, D., van den Broeke, M. R., Chan, W. L., Hu,  
 944 A., Beadling, R. L., Marsland, S. J., Mernild, S. H., Saenko, O. A., Swingedouw, D., Sullivan, A. and Yin, J.:  
 945 Fate of the Atlantic Meridional Overturning Circulation: Strong decline under continued warming and  
 946 Greenland melting, *Geophysical Research Letters*, 43, 12,252–12,260, doi:10.1002/2016GL070457, 2016.
- 947 Bennartz, R., Shupe, M. D., Turner, D.D., Walden, V. P., Steffen, K., Cox, C. J., Kulie, M. S., Miller, N. B. and  
 948 Pettersen, C.: July 2012 Greenland melt extent enhanced by low-level liquid clouds, *Nature* 496, 83-86, doi:  
 949 10.1038/nature120002, 2013.
- 950 Bonelli, S., Charbit, S., Kageyama, M., Woillez, M.-N., Ramstein, G., Dumas, C. and Quiquet A.: Investigating  
 951 the evolution of major Northern Hemisphere ice sheets during the last glacial cycle, *Climate of the Past*, 5,  
 952 329-245, doi: 10.5194/cp-5-329-2009, 2009.
- 953 Boone, A., and Etchevers, P.: An intercomparison of three snow schemes of varying complexity coupled to the  
 954 same land surface model: Local-scale evaluation at an Alpine site. *Journal of Hydrometeorology*, 2(4), 374-  
 955 394, 2001.
- 956 Boucher, O., Servonnat, J., Albright, A. L., Aumont, O., Balkanski, Y., Bastrikov, V., et al.: Presentation and  
 957 evaluation of the IPSL-CM6A-LR climate model, *Journal of Advances in Modeling Earth Systems*, 12,  
 958 e2019MS002010, doi: 10.1029/2019MS002010, 2020.
- 959 Bougamont, M., Bamber, J. L., Ridley, J. K., Gladstone, R. M., Greuell, W., Hanna, E., Payne, A. J and Rutt, I.:  
 960 Impact of model physics on estimating the surface mass balance of the Greenland ice sheet, *Geophysical*  
 961 *Research Letters*, 34, L17501, doi:10.1029/2007GL030700, 2007.
- 962 Born, A., Imhof, M. A., and Stocker, T. F.: An efficient surface energy-mass balance model for snow and ice, *The*  
 963 *Cryosphere*, 13, 1529-1546, doi: 10.5194/tc-13-1529-2019, 2019.
- 964 Box, J. E., Fettweis, X., Stroeve, J. C., Tedesco, M., Hall, D. K., and Steffen, K.: Greenland ice sheet albedo  
 965 feedback: thermodynamics and atmospheric feedbacks, *The Cryosphere*, 6, 821-839, doi: 10.5194/tc-821-  
 966 2012, 2012.
- 967 Box, J. E., van As, D., and Steffen, K.: Greenland, Canadian and Icelandic land-ice albedo grids (2000–2016),  
 968 *GEUS Bulletin*, 38, 53–56, doi: 10.34194/geusb.v38.4414, 2017.
- 969 Brun, E., Martin, E., Simon, V., Gendre, C. and Coleou, C.: An energy and mass model of snow cover suitable for  
 970 operational avalanche forecasting, *Journal of Glaciology*, 35 (121), 333-342, doi:  
 971 10.3189/S0022143000009254, 1989.
- 972 Brun, E., David, P., Sudul, M., and Brunot, G.: A numerical model to simulate snow cover stratigraphy for  
 973 operational avalanche forecasting, *Journal of Glaciology*, 38 (128), 13–22, doi: 10.3189/S0022143000009552,  
 974 1992.



- 975 Chalita, S. and Le Treut, H.: The albedo of temperate and boreal forest and the Northern Hemisphere climate: a  
 976 sensitivity experiment using the LMD GCM, *Climate Dynamics*, 10, 231-240, doi: 10.1007/BF00208990,  
 977 1994.
- 978 Charbit, S., Kageyama, M., Roche, D., Ritz, C; and Ramstein, G.: Investigating the mechanisms leading to the  
 979 deglaciation of past continental Northern hemisphere ice sheets with the CLIMBER-GREMLINS coupled  
 980 model, *Global and Planetary changes*, 48, 253-273, doi: 10.1016/j.gloplacha.2005.01.002, 2005.
- 981 Charbit, S., D. Paillard, and G. Ramstein (2008), Amount of CO<sub>2</sub> emissions irreversibly leading to the total melting  
 982 of Greenland, *Geophysical Research Letters*, 35, L12503, doi:10.1029/2008GL033472, 2008.
- 983 Charbit, S., Dumas, C., Kageyama, M., Roche, D. M. and Ritz, C.: Influence of ablation-related processes in the  
 984 build-up of Northern Hemisphere ice sheets during the last glacial cycle, *The Cryosphere*, 7, 681-698, doi:  
 985 10.5194/tc-7-681-2013, 2013.
- 986 Cheruy, F., Ducharne, A., Hourdin, F., Musat, I., Vignon, É., Gastineau, G., et al.: Improved near-surface  
 987 continental climate in IPSL-CM6A-LR by combined evolutions of atmospheric and land surface physics,  
 988 *Journal of Advances in Modeling Earth Systems*, 12, e2019MS002005., doi: 10.1029/2019MS002005, 2020.
- 989 Colbeck, S. C.: Theory of metamorphism of dry snow, *Journal of Geophysical Research*, 88(C9), 5475-5482, 1983
- 990 Cristea, N. C., Bennett, A., Nijssen, B. and Lundquist, J. D.: When and where are multiple snow layers important  
 991 for simulations of snow accumulation and melt? *Water Resources Research*, 58, e2020WR028993, doi:  
 992 10.1029/2020WR028993, 2022.
- 993 Cullather, R.I., Nowicki, S.M.J., Zhao, B. and Suarez, M.J.: Evaluation of the Surface Representation of the  
 994 Greenland Ice Sheet in a General Circulation Model, *Journal of Climate*, 27(13), 4835–4856, doi:10.1175/jcli-  
 995 d-13-00635.1, 2014.
- 996 Decharme, B., Brun, E., Boone, A., Delire, C., Le Moigne, P. and Morin., S.: Impacts of snow and organic soils  
 997 parameterization on northern Eurasian soil temperature profiles simulated by the ISBA land surface model,  
 998 *The Cryosphere*, 10, 853\_877, doi: 10.5194/tc-10-853-2016, 2016.
- 999 Dee, D. P., Uppala, S. M., Simmons, A. J., Berrisford, P., Poli, P., Kobayashi, S., Andrae, U., Balmaseda, M.A.,  
 1000 Balsamo, G., Bauer, P., Bechtold, P., Beljaars, A., C., M., van de Berg, L., Bidlot, J., Bormann, N., Delsol, C.,  
 1001 Dragani, R., Fuentes, M., Geer, A.J., Haimberger, L., Healy, S. B., Hersbach, H., Hólm, E.V., Isaksen, L.,  
 1002 Kallberg, P., Köhler, M., Matricardi, M., McNally, A.P., Monge-Sanz, B. M., Morcrette, J.-J., Park, B.-K.,  
 1003 Peubey, C., de Rosnay, P., Tavolato, C., Thépaut, J.-N. and Vitart, F.: The ERA-Interim reanalysis:  
 1004 configuration and performance of the data assimilation system. *Quarterly Journal of the Royal Meteorological*  
 1005 *Society*, 137, 553–597, doi:10.1002/qj.828, 2011.
- 1006 Delhasse, A., Kittel, C., Amory, C., Hofer, S., van As, D., S. Fausto, R., and Fettweis, X.: Brief communication:  
 1007 Evaluation of the near-surface climate in ERA5 over the Greenland Ice Sheet, *The Cryosphere*, 14, 957–965,  
 1008 doi:10.5194/tc-14-957-2020, 2020.
- 1009 De Ridder, K, and Schayes G: The IAGL land surface model: *Journal of Applied Meteorology*, 36, 167-182,  
 1010 doi:10.1086/451461, 1997.
- 1011 Dietrich, L. J., Steen-Larsen, H. C., Wahl, S., Faber, A.-K., and Fettweis, X.: On the importance of the humidity  
 1012 flux for the surface mass balance in the accumulation zone of the Greenland Ice Sheet, *The Cryosphere*, 18,  
 1013 289–305, doi: 10.5194/tc-18-289-2024, 2024.
- 1014 Domine, F., Picard, G., Morin, S., Barrere, M., Madore, J.-B., & Langlois, A.: Major issues in simulating some  
 1015 Arctic snowpack properties using current detailed snow physics models: Consequences for the thermal  
 1016 regime and water budget of permafrost, *Journal of Advances in Modeling Earth Systems*, 11, 34–44.  
 1017 <https://doi.org/10.1029/2018MS001445>, 2019.
- 1018 Dutra, E. Balsamo, E., Viterbo, P., Miranda, P. M. A., Beljaars, A., Schär, C. and Elder, K.: An Improved Snow  
 1019 Scheme for the ECMWF Land Surface Model: Description and Offline Validation, *Journal of*  
 1020 *Hydrometeorology*, 11(4); 899-916, doi: 10.1175/2010JHM1249.1, 2010.

- 1021 Edwards, T. L., Fettweis, X., Gagliardini, O., Gillet-Chaulet, F., Goelzer, H., Gregory, J. M., Hoffman, M.,  
 1022 Huybrechts, P., Payne, A.J., Perego, M., Price, S., Quiquet, A. and Ritz, C.: Effect of uncertainty in surface  
 1023 mass balance–elevation feedback on projections of the future sea level contribution of the Greenland ice sheet,  
 1024 *The Cryosphere*, 8, 195-208, doi: 10.5194/tc-8-195-2014, 2014.
- 1025 Enderlin, E. M., Howat, I. M., Jeong, S. Noh, M.-J., van Angelen, J. H. and van den Broeke, M. R. An improved  
 1026 mass budget for the Greenland ice sheet, *Geophysical Research Letters*, 41, 866–872,  
 1027 doi:10.1002/2013GL059010, 2014.
- 1028 Eyring, V., Bony, S. Meehl, G. A. Senior, C. A., Stevens, B., Stouffer, R. and Taylor, K. E.: Overview of the  
 1029 Coupled Model Intercomparison Project Phase 6 (CMIP6) experimental design and organization, *Geoscientific*  
 1030 *Model Development*, 9, 1937-1958, doi: 10.5194/gmd-9-1937-2016, 2016.
- 1031 Fausto, R. S., van As, D., Mankoff, K. D., Vandecrux, B., Citterio, M., Ahlstrøm, A. P., et al.: Programme for  
 1032 Monitoring of the Greenland Ice Sheet (PROMICE) automatic weather station data, *Earth System Scientific*  
 1033 *Data*, 13, 3819-3845, doi: 10.5194/essd-13-3819-2021, 2021.
- 1034 Fettweis, X., Box, J. E., Agosta, C., Amory, C., Kittel, C., Lang, C., van As, D., Machguth, H., and Gallée, H.:  
 1035 Reconstructions of the 1900–2015 Greenland ice sheet surface mass balance using the regional climate MAR  
 1036 model, *The Cryosphere*, 11, 1015–1033, <https://doi.org/10.5194/tc-11-1015-2017>, 2017.
- 1037 Fettweis, X. Hofer, S., Krebs-Kanzow, U., Amory, C., Aoki, T., Berends, C. J., et al.: GrSMBMIP:  
 1038 Intercomparison of the modelled 1980-2012 surface mass balance over the Greenland Ice sheet, *The*  
 1039 *Cryosphere*, 14, 3935-3958, doi: 10.5194/tc-14-3935-2020, 2020.
- 1040 Flanner, M. G., and C. S. Zender: Linking snowpack microphysics and albedo evolution, *Journal of Geophysical*  
 1041 *Research.*, 111, D12208, doi:10.1029/2005JD006834.
- 1042 Fox-Kemper, B., H.T. Hewitt, C. Xiao, G. Aðalgeirsdóttir, S.S. Drijfhout, T.L. Edwards, N.R. Golledge, M.  
 1043 Hemer, R.E. Kopp, G. Krinner, A. Mix, D. Notz, S. Nowicki, I.S. Nurhati, L. Ruiz, J.-B. Sallée, A.B.A.  
 1044 Slangen, and Y. Yu: Ocean, Cryosphere and Sea Level Change. *In Climate Change 2021: The Physical Science*  
 1045 *Basis. Contribution of Working Group I to the Sixth Assessment Report of the Intergovernmental Panel on*  
 1046 *Climate Change* [Masson-Delmotte, V., P. Zhai, A. Pirani, S.L. Connors, C. Péan, S. Berger, N. Caud, Y. Chen,  
 1047 L. Goldfarb, M.I. Gomis, M. Huang, K. Leitzell, E. Lonnoy, J.B.R. Matthews, T.K. Maycock, T. Waterfield,  
 1048 O. Yelekçi, R. Yu, and B. Zhou (eds.)]. Cambridge University Press, Cambridge, United Kingdom and New  
 1049 York, NY, USA, pp. 1211–1362, doi:10.1017/9781009157896.011, 2021.
- 1050 Franco, B., Fettweis, X., Lang, C., and Ericum, M.: Impact of spatial resolution on the modelling of the Greenland  
 1051 ice sheet surface mass balance between 1990–2010, using the regional climate model MAR, *The Cryosphere*,  
 1052 6, 695–711, doi: 10.5194/tc-6-695-2012, 2012.
- 1053 Fréville, H : Observation et simulation de la température de surface en Antarctique : application à l'estimation de  
 1054 la densité superficielle de la neige. (PhD), Université Paul Sabatier, Toulouse III, Toulouse. Retrieved from  
 1055 <https://tel.archives-ouvertes.fr/tel-01512722>, 2015.
- 1056 Fyke, J., Sergienko, O., Löfverström, M., Price, S. and Lenaerts, J. T., M.: An overview of interactions and  
 1057 feedbacks between ice sheets and the Earth system, *Review of Geophysics*, 56, doi: 10.1029/2018GR000600,  
 1058 2018.
- 1059 Gallée, H. and Schayes, G.: Development of a three-dimensional meso-primitive equations model: Katabatic winds  
 1060 simulation in the area of Terra Nova Bay, Antarctica, *Monthly Weather Review*, 122, 671–685, doi:  
 1061 10.1175/1520-0493(1994)122%3C0671:DOATDM%3E2.0.CO;2, 1994.
- 1062 Hahn, L. C., Storelvmo, T., Hofer, S., Parfitt, R. and Ummenhofer, C. C.: Importance of orography for Greenland  
 1063 ice sheet cloud and melt response to atmospheric blocking, *Journal of Climate*, 33, 4187-4206, doi:  
 1064 10.1175/JCLI-D-19\_0527.1, 2020.
- 1065 Hall, D. and Riggs, G.: MODIS/Terra Snow Cover Daily L3 Global 500m Grid, Version 6. Greenland coverage.,  
 1066 National Snow and Ice Data Center, NASA Distributed Active Archive Center, Boulder, Colorado USA.,  
 1067 <http://nsidc.org/data/MOD10A1/versions/6>, accessed December 2016., 2016.

- 1068 Hall, D. K., Riggs, G. A., and Salomonson, V. V.: Development of methods for mapping global snow cover using  
 1069 moderate resolution imaging spectroradiometer data, *Remote sensing of Environment*, 54, 127–140, doi:  
 1070 10.1016/0034-4257(95)00137-P, 1995, 1995.
- 1071 He, C., Flanner, M., Lawrence, D. M., and Gu, Y.: New features and enhancements in community land model  
 1072 (CLM5) snow albedo modeling: Description, sensitivity, and evaluation, *Journal of Advances in Modeling  
 1073 Earth Systems*, 16, e2023MS003861, doi: org/10.1029/2023MS003861, 2024.
- 1074 Helsen, M. M., van de Wal, R. S. W., Reerink, T. J., Bintanja, R., Madsen, M. S., Yang, S., Li, Q., and Zhang, Q.:  
 1075 On the importance of the albedo parameterization for the mass balance of the Greenland ice sheet in EC-Earth,  
 1076 *The Cryosphere*, 11, 1949–1965, doi: 10.5194/tc-11-1949-2017, 2017.
- 1077 Hersbach, H., Bell, B., Berrisford, P., Hirahara, S., Horányi, A., Muñoz-Sabater, J., Nicolas, J., Peubey, C., Radu,  
 1078 R., Schepers, D., Simmons, A., Soci, C., Abdalla, S., Abellan, X., Balsamo, G., Bechtold, P., Biavati, G.,  
 1079 Bidlot, J., Bonavita, M., De Chiara, G., Dahlgren, P., Dee, D., Diamantakis, M., Dragani, R., Flemming, J.,  
 1080 Forbes, R., Fuentes, M., Geer, A., Haimberger, L., Healy, S., Hogan, R.J., Hólm, E., Janisková, M., Keeley,  
 1081 S., Laloyaux, P., Lopez, P., Lupu, C., Radnoti, G., de Rosnay, P., Rozum, I., Vamborg, F., Villaume, S. and  
 1082 Thépaut, J.-N.: The ERA5 global reanalysis. *Quarterly Journal of the Royal Meteorological Society*, 146,  
 1083 1999–2049. doi: 10.1002/qj.3803, 2020.
- 1084 Hourdin, F., Musat, I., Bony, S., Braconnot, P., Codron, F., Dufresne, J., Fairhead, L., Filiberti, M., Friedlingstein,  
 1085 P., Grandpeix, J., Krinner, G., Le Van, P., Li, Z.-X., and Lott, F.: The LMDZ4 general circulation model:  
 1086 climate performance and sensitivity to parametrised physics with emphasis on tropical convection, *Climate  
 1087 Dynamics*, 27, 787–813, doi:10.1007/s00382-006-0158-0, 2006.
- 1088 Kageyama, M., Charbit, S., Ritz, C., Khodri, M. and Ramstein G.: Quantifying ice-sheet feedbacks during the last  
 1089 glacial inception, *Geophysical Research Letters*, 31, L24203, doi:10.1029/2004GL021339, 2004.
- 1090 Kojima, K.: Densification of seasonal snow cover. *Physics of Snow and Ice: Proceedings of the International  
 1091 Conference on Low Temperature Science, Part 1*, Sapporo, Japan, Hokkaido University, 1 (2), 929–952, 1967.
- 1092 Kokhanovsky, A. A. and Zege, E. P.: Scattering optics of snow, *Applied Optics*, 43, 1589–1602, 2004.
- 1093 Krinner, G., Viovy, N., de Noblet-Ducoudré, N., Ogée, J., Polcher, J., Friedlingstein, P., Ciais, P., Sitch, S., and  
 1094 Prentice, I. C.: A dynamic global vegetation model for studies of the coupled atmosphere-biosphere system,  
 1095 *Global Biogeochemical Cycles*, 19, GB1015, doi:10.1029/2003GB002199, 2005.
- 1096 Lawrence, D. M., Fisher, R. A., Koven, C. D., Oleson, K. W., Swenson, S. C., Bonan, G., Collier, N., Ghimire,  
 1097 B., van Kampenhout, L., Kennedy, D., Kluzek, E., Lawrence, P. J., Li, F., Li, H., Lombardozzi, D., Riley, W.  
 1098 J., Sacks, W. J., Shi, M., Vertenstein, M., Wieder, W. R., Xu, C., Ali, A. A., Badger, A. M., Bisht, G., van den  
 1099 Broeke, M., Brunke, M. A., Burns, S. P., Buzan, J., Clark, M., Craig, A., Dahlin, K., Drewniak, B., Fisher, J.  
 1100 B., Flanner, M., Fox, A. M., Gentine, P., Hoffman, F., Keppel-Aleks, G., Knox, R., Kumar, S., Lenaerts, J.,  
 1101 Leung, L. R., Lipscomb, W. H., Lu, Y., Pandey, A., Pelletier, J. D., Perket, J., Randerson, J. T., Ricciuto, D.  
 1102 M., Sanderson, B. M., Slater, A., Subin, Z. M., Tang, J., Thomas, R. Q., Val Martin, M., and Zeng, X.: The  
 1103 Community Land Model Version 5: Description of New Features, Benchmarking, and Impact of Forcing  
 1104 Uncertainty, *Journal of Advances in Modeling Earth Systems.*, 11, 4245–4287, doi: 10.1029/2018MS001583,  
 1105 2019.
- 1106 Lefebre, F., Gallée, H., van Ypersele, J.-P. and W. Greuell, Modeling of snow and ice melt at ETH Camp (West  
 1107 Greenland): A study of surface albedo, *Journal of Geophysical Research*, 108(D8), 4231,  
 1108 doi:10.1029/2001JD001160, 2003.
- 1109 Libois, Q., Picard, G., France, J. L., Arnaud, L., Dumont, M., Carmagnola, C. M., and King, M. D.: Influence of  
 1110 grain shape on light penetration in snow, *The Cryosphere*, 7, 1803–1818, [https://doi.org/10.5194/tc-7-1803-](https://doi.org/10.5194/tc-7-1803-2013)  
 1111 2013, 2013.
- 1112 Louis, J. F.: A parametric model of vertical eddy fluxes in the atmosphere. *Boundary-Layer Meteorology*, 17(2),  
 1113 187-202, 1979.

- 1114 Lynch-Stieglitz, M.: The development and validation of a simple snow model for the GISS GCM, *Journal of*  
1115 *Climate*, 7, 1842-1855, doi: 10.1175/1520-0442(1994)007%3C1842:TDAVOA%3E2.0.CO;21994, 1994.
- 1116 Martin, T., Biastoch, A., Lohmann, G., Mikolajewicz, U., and Wang, X.: On timescales and reversibility of the  
1117 ocean's response to enhanced Greenland Ice Sheet melting in comprehensive climate models. *Geophysical*  
1118 *Research Letters*, 49, e2021GL097114. doi: 10.1029/2021GL097114, 2022.
- 1119 Machguth, H., Thomsen, H. H., Weidick, A., Abermann, J., Ahlström, A. P., Andersen, M. L., Andersen, S. B.,  
1120 Björk, A. A., Box, J. E., Braithwaite, R. J., Bøggild, C. E., Citterio, M., Clement, P., Colgan, W., Fausto, R.  
1121 S., Gleie, K., Hasholt, B., Hynek, B., Knudsen, N. T., Larsen, S. H., Mernild, S., Oerlemans, J., Oerter, H.,  
1122 Olesen, O. B., Smeets, C. J. P. P., Steffen, K., Stober, M., Sugiyama, S., van As, D., van den Broeke, M. R.,  
1123 and van de Wal, R. S.: Greenland surface mass balance observations from the ice sheet ablation area and local  
1124 glaciers, *Journal of Glaciology*, 62, 861–887, <https://doi.org/10.1017/jog.2016.75>, 2016.
- 1125 Maeno N.: The electrical behaviours of Antarctic ice drilled at Mizuho Station, East Antarctica *Memoirs of the*  
1126 *National Institute of Polar Research* 10, 77-94, 1978.
- 1127 Maeno, N., and Ebinuma, T.: Pressure sintering of ice and its implication to the densification of snow at polar  
1128 glaciers and ice sheets, *Journal of Physical Chemistry*, 87, 4103-4110, 1983.
- 1129 Mankoff, K. D., Fettweis, X., Langen, P. L., Stendel, M., Kjeldsen, K. K., Karlsson, N. B., Noël, B., van den  
1130 Broeke, M. R., Solgaard, A., Colgan, W., Box, J. E., Simonsen, S. B., King, M. D., Ahlstrøm, A. P., Andersen,  
1131 S. B., and Fausto, R. S.: Greenland ice sheet mass balance from 1840 through next week, *Earth Syst. Sci. Data*,  
1132 13, 5001–5025, <https://doi.org/10.5194/essd-13-5001-2021>, 2021.
- 1133 Marshall, H.P., Conway, H., Rasmussen, L.A.: Snow densification during rain, *Cold Regions Science and*  
1134 *Technology*, 30, 35-41, doi: 10.1016/S0165-232X(99)00011-7, 1999.
- 1135 Mellor, M.: Snow and Ice on the Earth's Surface, *Cold regions science and engineering. Part 2, Physical science.*  
1136 *Sect. C, The physics and mechanics of ice Snow and Ice on the Earth's Surface*, U.S. Army Materiel Command,  
1137 Cold Regions Research and Engineering Laboratory, 163pp., 1964.
- 1138 Mizukami, N., and Perica, S.: Spatiotemporal characteristics of snowpack density in the mountainous regions of  
1139 the western United States. *Journal of Hydrometeorology*, 9(6), 1416–1426.  
1140 <https://doi.org/10.1175/2008JHM981.1>, 2008.
- 1141 Monin, A. S., and Obukhov, A. M.: Basic laws of turbulent mixing in the surface layer of the atmosphere. *Contrib.*  
1142 *Geophys. Inst. Acad. Sci. USSR*, 151(163), e187, 1954.
- 1143 Montgomery L, Koenig L, Lenaerts JTM, Kuipers Munneke P (2020). Accumulation rates (2009–2017) in  
1144 Southeast Greenland derived from airborne snow radar and comparison with regional climate models. *Annals*  
1145 *of Glaciology* 61(81), 225–233, doi: 10.1017/aog.2020.8, 2020.
- 1146 Muntjewerf, L., Sellevod, R., Vizcaino, M., Ernani da Silva, C., Petrini, M., Thayer-Calder, K., Scherrenberg, M.  
1147 D. W., Bradley; S. L., Katsman, C. A., Fyke, J., Lipscomb, W. H., Löfverström, M. and Sacks, W.J.:  
1148 Accelerated Greenland ice sheet mass loss under high greenhouse gas forcing as simulated by the coupled  
1149 CESM2.1-CISM2.1, *Journal of Advances Modeling in Earth Systems*, 12, e2019MS002031, doi:  
1150 10.1029/2019MS002031, 2020.
- 1151 Niu, G.-Y., and Yang, Z.-L.: An observation-based formulation of snow cover fraction and its evaluation over  
1152 large North American river basins, *Journal of Geophysical Research*, 112, D21101,  
1153 doi:10.1029/2007JD008674, 2007.
- 1154 Noël, B., van de Berg, W. J., Machguth, H., Lhermitte, S., Howat, I., Fettweis, X., and van den Broeke, M. R.: A  
1155 daily, 1 km resolution data set of downscaled Greenland ice sheet surface mass balance (1958–2015), *The*  
1156 *Cryosphere*, 10, 2361–2377, <https://doi.org/10.5194/tc-10-2361-2016>, 2016.
- 1157 Noël, B., van de Berg, W. J., van Wessem, J. M., van Meijgaard, E., van As, D., Lenaerts, J. T. M. Lhermitte, S.,  
1158 Kuipers Munneke, P., Smeets, C. J. P. P., van Ulft, L.H., van de Wal, R. S. W., and van den Broeke, M. R.:

- 1159 Modelling the climate and surface mass balance of polar ice sheets using RACMO2 – Part 1: Greenland (1958–  
1160 2016), *The Cryosphere*, 12, 811–831, <https://doi.org/10.5194/tc-12-811-2018>, 2018.
- 1161 Pahaut, E.: La métamorphose des cristaux de neige (Snow crystal metamorphosis), *Monographies de la*  
1162 *Météorologie Nationale*, No. 96, Météo France, Direction de la météorologie nationale, France, 58pp., 1976.
- 1163 Patterson, W. S. B., *The Physics of Glaciers*, Butterworth-Heinemann, 1994.
- 1164 Punge, H. J., Gallée, H., Kageyama, M. and Krinner, G.: Modelling snow accumulation on Greenland in Eemian,  
1165 glacial inception, and modern climates in a GCM, *Climate of the Past*, 8, 1801–1819, doi: 10.5194/cp-8-1801-  
1166 2012, 2012, 2012.
- 1167 Raoult, N., Charbit, S., Dumas, C., Maignan, F., Ottlé, C., and Bastrikov, V.: Improving modelled albedo over the  
1168 Greenland ice sheet through parameter optimisation and MODIS snow albedo retrievals, *The Cryosphere*, 17,  
1169 2705–2724, <https://doi.org/10.5194/tc-17-2705-2023>, 2023.
- 1170 Reeh, N.: Parameterization of melt rate and surface temperature on the Greenland ice sheet, *Polarforschung*, 5913,  
1171 113-128, 1991.
- 1172 Reynolds, C. A., Jackson, T. J., and Rawls, W. J.: Estimating soil water-holding capacities by linking the Food  
1173 and Agriculture Organization soil map of the world with global pedon databases and continuous pedotransfer  
1174 functions, *Water Resources Research*, 36, 3653–3662, doi: 10.1029/2000WR900130, 2000.
- 1175 Ridley, J. K., Huybrechts, P., Gregory, J. M. and Lowe, J. A.: Elimination of the Greenland ice sheet in a high  
1176 CO<sub>2</sub> climate, *Journal of Climate*, 18, 3409-3427, doi: 10.1175/JCLI3482.1, 2005.
- 1177 Riihelä, A., King, M. D. and Anttila K.: The surface albedo of the Greenland ice sheet between 1982 and 2015  
1178 from CLARA-A2 dataset and its relationship to the ice sheet's surface mass balance, *The Cryosphere*, 13,  
1179 2597-2614, doi: 10.5194/tc-13-2597-2019, 2019.
- 1180 Roche, D. M., Dumas, C., Bügelmayer, M., Charbit, S. and Ritz, C.: Adding a dynamical cryosphere to  
1181 iLOVECLIM (version 1.0): coupling with the GRISLI ice-sheet model, *Geoscientific Model Development*, 7,  
1182 1377-1394, doi: 10.5194/gmd-7-1377-2014, 2014.
- 1183 Ryan, J.V., Smith, L. C., van As, D., Cooley, S. W., Cooper, M. G., Pitcher, L. H., and Hubbard, A.: Greenland  
1184 Ice Sheet surface melt amplified by snowline migration and bare ice exposure, *Science Advances*, 5, eaav3738,  
1185 doi: 10.1126/sciadv.aav3738, 2019.
- 1186 Sellevod, R., van Kampenhout, L., Lenaerts, J. T. M., Noël, B., Lipscomb, W. H. and Vizcaino, M.: Surface mass  
1187 balance downscaling through elevation classes in an Earth system model: application to the Greenland ice  
1188 sheet, *The Cryosphere*, 13, 3193-3208, doi: 10.5194/tc-13-3193-2019, 2019.
- 1189 Smith, R. S., Mathiot P., Siahaan, A., Lee, V., Cornford, S. L., Gregory, J. M., Payne, A. J., Jenkins, A., Holland,  
1190 P., R., Ridley, J. K. and Jones, C. G.: Coupling the U.K. Earth System Model to dynamic models of the  
1191 Greenland and Antarctic ice sheets, *Journal of Advances Modeling in Earth Systems*, 13, e2021MS002520,  
1192 doi: 10.1029/2021MS002520, 2021.
- 1193 Smith, B. E., Medley, B., Fettweis, X., Sutterley, T., Alexander, P., Porter, D., and Tedesco, M.: Evaluating  
1194 Greenland surface-mass-balance and firn-densification data using ICESat-2 altimetry, *The Cryosphere*, 17,  
1195 789–808, doi: 10.5194/tc-17-789-2023, 2023.
- 1196 Stephens, M. A.: Use of the Kolmogorov-Smirnov, Cramer-von Mises and related statistics without extensive  
1197 tables, *Journal of the Royal Statistical Society Series B (Methodological)*, 32 (1), 115-122, 1970.
- 1198 Sun, S., Jin, J. and Xue, Y.: A simple snow-atmosphere-soil transfer model, *Journal of Geophysical Research*, 104  
1199 (D16), 19587-19597, doi: 10.1029/1999JD900305, 1999.
- 1200 Taylor, K. E., Stouffer, R. J. and Meehl, G. A.: An overview of CMIP5 and the experiment design, *Bulletin of*  
1201 *American Meteorological Society*, 93, 485-498, doi: 10.1175/BAMS-D-11-00094.1, 2012.

- 1202 Tedesco, M. and Fettweis, X.: Unprecedented atmospheric conditions (1948–2019) drive the 2019 exceptional  
 1203 melting season over the Greenland ice sheet, *The Cryosphere*, 14, 1209–1223, [https://doi.org/10.5194/tc-14-](https://doi.org/10.5194/tc-14-1209-2020)  
 1204 1209-2020, 2020.
- 1205 The IMBIE team: Mass balance of the Greenland ice sheet from 1992 to 2018, *Nature*, 579, 233-239, doi:  
 1206 10.1038/s41586-019-1855-2, 2020.
- 1207 Uppala, S.M., Kållberg, P.W., Simmons, A.J., Andrae, U., da Costa Bechtold, V., Fiorino, M., Gibson, J.K.,  
 1208 Haseler, J., Hernandez, A., Kelly, G.A., Li, X., Onogi, K., Saarinen, S., Sokka, N., Allan, R.P., Andersson, E.,  
 1209 Arpe, K., Balmaseda, M.A., Beljaars, A.C.M., van de Berg, L., Bidlot, J., Bormann, N., Caires, S., Chevallier,  
 1210 F., Dethof, A., Dragosavac, M., Fisher, M., Fuentes, M., Hagemann, S., Hólm, E.V., Hoskins, B.J., Isaksen,  
 1211 L., Janssen, P.A.E.M., Jenne, R., McNally, A.P., Mahfouf, J.-F., Morcrette, J.-J., Rayner, N.A., Saunders,  
 1212 R.W., Simon, P., Sterl, A., Trenberth, K.E., Untch, A., Vasiljevic, D., Viterbo, P. and Woollen, J.: The ERA-  
 1213 40 re-analysis. *Quarterly Journal of the Royal Meteorological Society*, 131, 2961–3012, 2005.
- 1214 Urraca, R., Lanconelli, C., Cappucci, F., Gobron, N.: Comparison of Long-Term Albedo Products against Spatially  
 1215 Representative Stations over Snow, *Remote Sensing* 14, 3745, [doi: 10.3390/rs14153745](https://doi.org/10.3390/rs14153745), 2022.
- 1216 Urraca, R., Lanconelli, C., Cappucci, F., Gobron, N. : Assessing the fitness of satellite albedo products for  
 1217 monitoring snow albedo trends, *IEEE Transactions on geoscience and remote sensing*, 61, 4404817, doi:  
 1218 10.1109/TGRS2023.3281188, 2023.
- 1219 van Angelen, J. H., van den Broeke, M. R., and van de Berg, W. J.: Momentum budget of the atmospheric boundary  
 1220 layer over the Greenland ice sheet and its surrounding seas, *Journal of Geophysical Research-Atmosphere.*, 116,  
 1221 D10101, doi:10.1029/2010JD015485, 2011.
- 1222 van den Broeke, M., Bamber, J., Ettema, J., Rignot, E., Schrama, E., van de Berg, W. J., van Meijgaard, E.,  
 1223 Velicogna, I., Wouters, B.: Partitioning recent Greenland mass loss, *Science*, 326, 984-986, doi:  
 1224 10.1126/science1178276, 2009.
- 1225 van den Broeke, M., Enderlin, E. M., Howat, I. M., Kuipers Munnneke, P., Noël, B. P. Y., van de Berg, W. J., van  
 1226 Meijgaard, E., Wouters, B.: On the recent contribution of the Greenland ice sheet to sea level change, *The*  
 1227 *Cryosphere*, 10, 1933-1946, doi: 10.5194/tc-10-1933-2016, 2016.
- 1228 van de Wal, R., S., W.: Mass-balance modelling of the Greenland ice sheet: a comparison of an energy-balance  
 1229 and a degree-day model, *Annals of Glaciology*, 23, 36-45, 1996.
- 1230 Vionnet, V. Brun, E., Morin, S., Boone, A., Faroux, S., Le Moigne, P., Martin, E. and Willemet J.-M.: The detailed  
 1231 snowpack scheme Crocus and its implementation in SURFEX v7.2, *Geoscientific Model Development*, 5, 773-  
 1232 791, doi: 10.5194/gmd-5-773-2012, 2012.
- 1233 Vizcaino, M., Mikolajewicz, U., Jungclaus, J. and Schurgers, G.: Climate modification by future ice sheet changes  
 1234 and consequences for ice sheet mass balance, *Climate Dynamics*, 34, 301-324, doi: 10.1007/s00382-009-0591-  
 1235 y, 2010.
- 1236 Vizcaino, M., Lipscomb, W. H., Sacks, W. J., van Angelen, J. H., Wouters, B. and van den Broeke, M. R.:  
 1237 Greenland surface mass balance as simulated by the Community Earth System Model. Part I: Model evaluation  
 1238 and 1850-2005 results, *Journal of Climate*, 26, 7793-7812, doi: 10.1175/JCLI-D-00615.1, 2013.
- 1239 Vizcaino, M.: Ice sheets as interactive components of Earth System Models: progress and challenges, *WIREs*  
 1240 *Climate Change*, 5, 557–568. doi: 10.1002/wcc.285, 2014.
- 1241 Wang, T., Ottlé, C., Boone, A., Ciais, P., Brun, E., Morin, S., Krinner, G., Piao, S. and Peng, S.: Evaluation of an  
 1242 improved intermediate complexity snow scheme in the ORCHIDEE land surface model, *Journal of*  
 1243 *Geophysical Research Atmosphere*, 118, 6064–6079, doi:10.1002/jgrd.50395, 2013.
- 1244 Wang, T., Peng, S., Krinner, G., Ryder, J., Li, Y., Dantec-Nédélec, S. and Ottlé, C.: Impacts of Satellite-Based  
 1245 Snow Albedo Assimilation on Offline and Coupled Land Surface Model Simulations. *PLoS ONE* 10(9):  
 1246 e0137275, doi:10.1371/journal.pone.0137275, 2015.

- 1247 Wang, F., Cheruy, F., and Dufresne, J.-L.: The improvement of soil thermodynamics and its effects on land surface  
1248 meteorology in the IPSL climate model, *Geoscientific Model Development.*, 9, 363–381,  
1249 <https://doi.org/10.5194/gmd-9-363-2016>, 2016.
- 1250 Warren S.: Optical properties of snow. *Reviews of Geophysics and Space Physics*, 20(1), 67-89, 1982.
- 1251 Yang, Z., Chen, R., Liu, Y., Zhao, Y., Liu, Z., & Liu, J.: The impact of rain-on-snow events on the snowmelt  
1252 process: A field study, *Hydrological Processes*, 37(11), e15019; doi: 10.1002/hyp.15019, 2023.
- 1253 Yen, Y.-C.: Review of thermal properties of snow, ice and sea ice. *Cold Regions Research and Engineering*  
1254 *Laboratory*, Hanover, NH, 1981.